

Frequency multiplexed superconducting quantum interference device readout of large bolometer arrays for cosmic microwave background measurements

M.A. Dobbs¹, M. Lueker^{2,3}, K.A. Aird⁴, A.N. Bender⁵, B.A. Benson^{6,7}, L.E. Bleem^{6,8}, J.E. Carlstrom^{6,8,7,9}, C.L. Chang^{6,7}, H.-M. Cho¹⁰, J. Clarke^{2,11}, T.M. Crawford^{6,9}, A.T. Crites^{6,9}, D.I. Flanigan², T. de Haan¹, E.M. George², N.W. Halverson⁵, W.L. Holzapfel², J.D. Hrubes⁴, B.R. Johnson^{2,12}, J. Joseph¹³, R. Keisler^{6,8}, J. Kennedy¹, Z. Kermish², T.M. Lanting^{1,14}, A.T. Lee^{2,15}, E.M. Leitch^{6,9}, D. Luong-Van⁴, J.J. McMahon¹⁶, J. Mehl^{6,9}, S.S. Meyer^{6,8,7,9}, T.E. Montroy¹⁷, S. Padin^{3,6,7}, T. Plagge^{6,9}, C. Pryke¹⁸, P.L. Richards², J.E. Ruhl¹⁷, K.K. Schaffer^{19,6,7}, D. Schwan², E. Shirokoff^{2,3}, H.G. Spieler¹⁵, Z. Staniszewski^{17,3}, A.A. Stark²⁰, K. Vanderlinde¹, J.D. Vieira³, C. Vu¹³, B. Westbrook², R. Williamson^{6,9}

¹*Physics Department, McGill University, Montreal, Quebec H3A 2T8, Canada*

²*Physics Department, University of California, Berkeley, California 94720, USA*

³*Division of Physics, Math and Astronomy, California Institute of Technology, 1200 E. California Blvd., Pasadena, CA 91125*

⁴*University of Chicago, 5640 South Ellis Avenue, Chicago, IL 60637*

⁵*Department of Astrophysical and Planetary Sciences and Department of Physics, University of Colorado, Boulder, CO 80309*

⁶*Kavli Institute for Cosmological Physics, University of Chicago, 5640 South Ellis Avenue, Chicago, IL 60637*

⁷*Enrico Fermi Institute, University of Chicago, 5640 South Ellis Avenue, Chicago, IL 60637*

⁸*Department of Physics, University of Chicago, 5640 South Ellis Avenue, Chicago, IL 60637*

⁹*Department of Astronomy and Astrophysics, University of Chicago, 5640 South Ellis Avenue, Chicago, IL 60637*

¹⁰*National Institute of Standards and Technology, Boulder, Colorado 80305, USA*

¹¹*Materials Science Division, Lawrence Berkeley National Lab, Berkeley, California 94720, USA*

¹²*Department of Physics, Columbia University, 538 West 120th Street, New York, NY 10027*

¹³*Engineering Division, Lawrence Berkeley National Lab, Berkeley, California 94720, USA*

¹⁴*now at D-Wave Systems, Burnaby, British Columbia V5C 6G9, Canada*

¹⁵*Physics Division, Lawrence Berkeley National Lab, Berkeley, California 94720, USA*

¹⁷*Physics Department and CERCA, Case Western Reserve University, 10900 Euclid Ave., Cleveland, OH 44106*

¹⁶*Department of Physics, University of Michigan, 450 Church Street, Ann Arbor, MI, 48109*

¹⁸*University of Minnesota/Twin Cities, School of Physics and Astronomy, Minneapolis, MN, 55455*

¹⁹*Liberal Arts Department, School of the Art Institute of Chicago, 112 S Michigan Ave, Chicago, IL 60603*

²⁰*Harvard-Smithsonian Center for Astrophysics, 60 Garden Street, Cambridge, MA 02138*

(Dated: November 27, 2024)

A technological milestone for experiments employing Transition Edge Sensor (TES) bolometers operating at sub-kelvin temperature is the deployment of detector arrays with 100s–1000s of bolometers. One key technology for such arrays is readout multiplexing: the ability to read out many sensors simultaneously on the same set of wires. This paper describes a frequency-domain multiplexed readout system which has been developed for and deployed on the APEX-SZ and South Pole Telescope millimeter wavelength receivers. In this system, the detector array is divided into modules of seven detectors, and each bolometer within the module is biased with a unique \sim MHz sinusoidal carrier such that the individual bolometer signals are well separated in frequency space. The currents from all bolometers in a module are summed together and pre-amplified with Superconducting Quantum Interference Devices (SQUIDs) operating at 4 K. Room-temperature electronics demodulate the carriers to recover the bolometer signals, which are digitized separately and stored to disk. This readout system contributes little noise relative to the detectors themselves, is remarkably insensitive to unwanted microphonic excitations, and provides a technology pathway to multiplexing larger numbers of sensors.

PACS numbers: 07.20.Mc, 07.57.Kp, 95.55.Sh, 95.55.Rg

Keywords: SQUID, multiplexed readout, bolometer, mm-wavelength astronomy

I. INTRODUCTION

A new generation of mm-wavelength receivers instrumented with hundreds or thousands of transition edge sensor (TES) bolometric detectors, e.g., [1–5], is allowing for unprecedented precision in measurements of the Cosmic Microwave Background (CMB). Large TES arrays are expected to bring forth similar advances in other observational bands such as the sub-mm (e.g., [6]), X-ray (e.g., [7]), and gamma-ray (e.g., [8–10]) as well as

phonon detection in dark matter direct detection experiments (e.g., [11]).

TES detectors in the millimeter to far-IR range are approaching the photon statistics limit, meaning their noise performance is dominated by fluctuations in the arrival rate of photons at the detector, and not by the intrinsic noise performance of the detectors themselves. Consequently, higher mapping speed can best be realized by increasing the number of detectors, rather than by improving the detectors themselves. A key challenge in building focal planes with large sensor counts has been

multiplexing the signals between the cold sub-kelvin operating temperature of the detectors and room temperature electronics. Multiplexing minimizes the heat-load on the detector cold stage and reduces the complexity of the cold wiring.

Two complementary multiplexing strategies are commonly used: (1) time domain multiplexing (TDM) [12–15], where the detectors are read out sequentially one at a time with a revisit rate that is faster than the detector time constant, and (2) frequency-domain multiplexing (fMUX) where each detector is biased at a unique location in frequency space and read out continuously. While the TDM system was developed earlier, both technologies are now quite mature. An eight-channel TDM proof-of-concept system was first to make sky observations [16]. A new TES readout scheme that multiplexes signals from GHz frequency RF SQUIDS [17, 18] is in the early stages of development, as is a new code-domain multiplexing readout [19].

In this paper, we describe the fMUX readout system [20–27] as it has been deployed for mm-wavelength observations with the APEX-SZ [2, 28, 29] and South Pole Telescope (SPT) SZ [4, 30] receivers. These experiments are designed for high angular resolution observations of the CMB. For example, the unique combination of sensitivity and resolution of these instruments makes it possible to study the structure and evolution of galaxy clusters using the Sunyaev-Zel’dovich (SZ) effect [31], a small distortion imprinted on the CMB when primordial photons inverse-Compton scatter off hot electrons in the intra-cluster medium. The resolved SZ image of the Bullet Cluster (1E 0657-56) obtained with APEX-SZ [32] was the first published scientific result with a large array of multiplexed TES detectors. SPT achieved the first SZ detections of previously unknown galaxy clusters [33] with its array of multiplexed TES detectors. A wealth of new measurements have been presented by both SPT [34–46] and APEX-SZ [47–49].

Other implementations of frequency multiplexed TES readout systems are described in Refs. [50, 51].

This paper is outlined as follows. In §II, a brief overview of the system, its advantages, and the performance requirements is presented. A detailed description of the sub-kelvin components of the system is provided in §III. This description is accompanied by a summary of the design process for specifying the basic multiplexer parameters, such as channel spacing. §IV details the SQUID pre-amplifier and back-end electronics. The performance for the system operating in the SPT and APEX-SZ experiments is described in §V, and conclusions are presented in §VI.

II. GENERAL OVERVIEW

The fMUX readout system operates in concert with an array of TES detectors. Each bolometric detector has a metal absorber and TES, which are coupled by a weak

thermal link to a ~ 0.25 K thermal bath. A constant-amplitude sinusoidal voltage bias is applied to the TES, which is a superconducting film with a transition temperature of about 0.5 K. The combination of radiation power absorbed from the sky and electrical bias power raises the temperature of the TES mid-way into its superconducting transition. An increase in sky power incident on the absorber alters the TES resistance and (through negative electro-thermal feedback, see §III A), produces a decrease in the electrical power being dissipated in the sensor. This, in turn, produces a change in the current through the sensor, since the applied voltage is held constant. TES thermometers are chosen because their steep transition allows for linearity, their monolithic wafer-scale fabrication yields large arrays, and because their low impedance makes them compatible with multiplexing. The properties and parameters of the bolometer arrays dictate the design requirements for the readout system.

A. The APEX-SZ and SPT Experiments

The SPT focal plane [52, 55] is divided into three separate bands centered at approximately 95, 150, and 220 GHz, with bandwidths of about 40 GHz. The APEX-SZ detectors operate at 150 GHz with ~ 36 GHz bandwidth. Coherent amplification devices such as High Electron Mobility Transistors (HEMTs) are ultimately limited by quantum noise, and incoherent detection with bolometers can offer higher sensitivity at these frequencies.

Both experiments use a closed-cycle refrigerator manufactured by Chase Research Cryogenics (140 Manchester Road, Sheffield, UK S10 5DL), with two ^3He sorption stages and one ^4He sorption stage, to cool the bolometers and sub-kelvin multiplexer components to their ~ 0.25 K bath temperature. The refrigerator is thermally coupled to the ~ 4 K stage of a Cryomech (113 Falso Drive, Syracuse, USA 13211) model PT 410 mechanical pulse tube cooler. With this combination, the system is cooled without the use of any expendable cryogenics, greatly simplifying the operation of these instruments in the remote environments of the Chilean Atacama plateau and the geographic South Pole for APEX-SZ and SPT respectively.

APEX-SZ and SPT have 0.4° and 1° fields of views (FoVs) respectively, and both experiments have full width half maximum (FWHM) beam sizes of about 1 arcminute. There are no “chopper mirrors” in the optical systems to modulate the beams across the sky; instead the telescopes are scanned at typical speeds of 0.25 – 0.5° /second. Since we are interested in observing astronomical structures (such as primary CMB fluctuations) at scales occupying a large fraction of the FoV, these experimental parameters and scan strategy dictate that information will appear in the detector timestreams at frequencies as low as $\lesssim 1$ Hz.

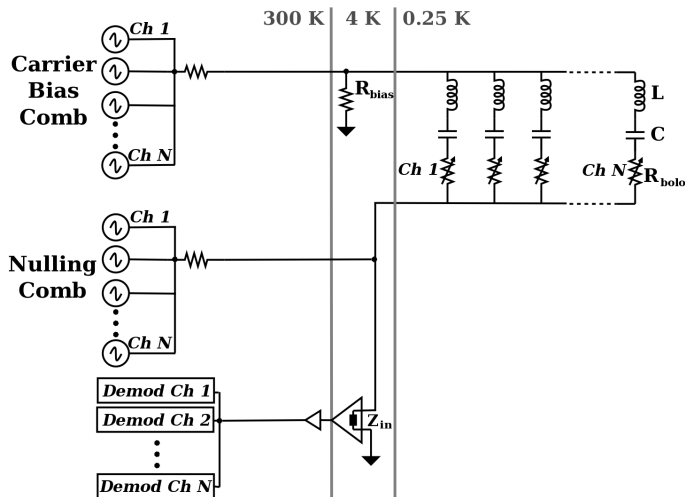


FIG. 1: Layout of the frequency-domain multiplexed readout for a module of N TES detectors.

B. Readout System Concept

The detector readout is segregated into identical fMUX modules, each biasing and reading out N TES detectors on a single pair of wires. The basic layout of one multiplexer module of the fMUX system is shown in Figure 1. Figure 2 shows the system electronics (§ IV) in greater detail. To set its specific bias frequency, each TES bolometer (R_{bolo}) is connected through a series-resonant circuit formed by an inductor (L) and capacitor (C) on the sub-kelvin stage. The inductance is the same for all channels, defining the same $R_{\text{bolo}}/(2\pi L)$ electrical bandwidth for each detector. Thus, changing the capacitance alone sets the LCR_{bolo} channel resonant frequency. A bank of N fixed amplitude sine-wave generators operating at room temperature provides a ‘comb’ of detector voltage bias carriers, each operating at a frequency tuned to match the resonance of the individual LCR_{bolo} channels. Sky signals modulate the TES resistance, amplitude modulating the current of the carrier. This encodes the sky-signal in symmetrical sidebands above and below the carrier. Since the signal currents from the individual TES detectors are at different frequencies, they can all be summed together and transmitted to a single low-impedance input amplifier operating at 4 K. We employ a series array SQUID operating in a flux-locked loop (FLL) for this transimpedance amplification stage. To reduce the SQUID dynamic range requirements, an inverted version of the carrier comb, referred to as the ‘nulling comb’, is injected at the SQUID input to cancel the carriers (see § IV). The comb of amplitude modulated carriers is transmitted from the SQUID output to a bank of room temperature demodulators. There is separate analog demodulator for each TES that mixes the detector signal down to baseband. A low-pass anti-aliasing filter is applied to the resultant timestream before it is digitized. The signal amplitude is proportional to the photon power

deposited on the TES photon absorber. The APEX-SZ and SPT systems are configured with $N = 7$ detectors per readout module.

The configuration shown in Figure 1 uses current summing at the low impedance input of the transimpedance amplifier using a SQUID input stage. The fMUX can also be implemented by introducing a transformer in series with each bolometer, and summing the voltages from the transformer secondaries [21], but since a TES biased by a constant voltage yields changes in signal current, the current summing configuration is more direct. The design requirements, challenges, and implications are similar for both configurations. For simplicity, we focus only on the current summing strategy.

The fMUX readout architecture has the following key features:

- (1) Simplicity of cryogenic components: the sub-kelvin components consist of one capacitor and one superconducting inductor per bolometer, followed by a single SQUID pre-amplifier per readout module at 4K. Since the SQUIDS are located far from the detectors, they can be magnetically shielded in a straightforward manner. The only custom sub-kelvin components are the inductors, which can be manufactured via a simple, low cost process with high yield.
- (2) Low wire count per detector and independent modules. The fMUX requires just two wires per readout module for both bias and readout. Each module is completely independent so that wiring failures or other defects in one module do not affect others.
- (3) Signals are modulated at high (typically MHz) frequencies, well above microphonic pickup frequencies and amplifier low-frequency noise. The inductor-capacitor filters in series with the detectors suppress currents at frequencies outside the narrow LCR_{bolo} bandwidth of the individual bolometer legs. This reduces crosstalk, eliminates the dominant source of microphonics usually present in bolometer systems, and results in a high rejection of electromagnetic interference that comes from numerous sources such as scan-correlated changes in magnetic field.
- (4) The readout system dissipates zero power on the detector cold stage as there are no resistive or active elements.
- (5) Channels are read out continuously with no switching transients that limit the detector bandwidth. This makes the system easily applicable to higher bandwidth application such as photon counting X-ray microcalorimeters.
- (6) The voltage bias can be set to optimize the sensitivity of each individual detector. This allows the readout system to compensate for detector fabrication non-uniformity.

Practical challenges for implementing the fMUX system include: achieving the large dynamic range needed to accommodate the bias carriers; meeting the strict stability requirements on the bias generators needed to avoid introducing low frequency noise; managing non-idealities in cryogenic wiring that can introduce stray inductances

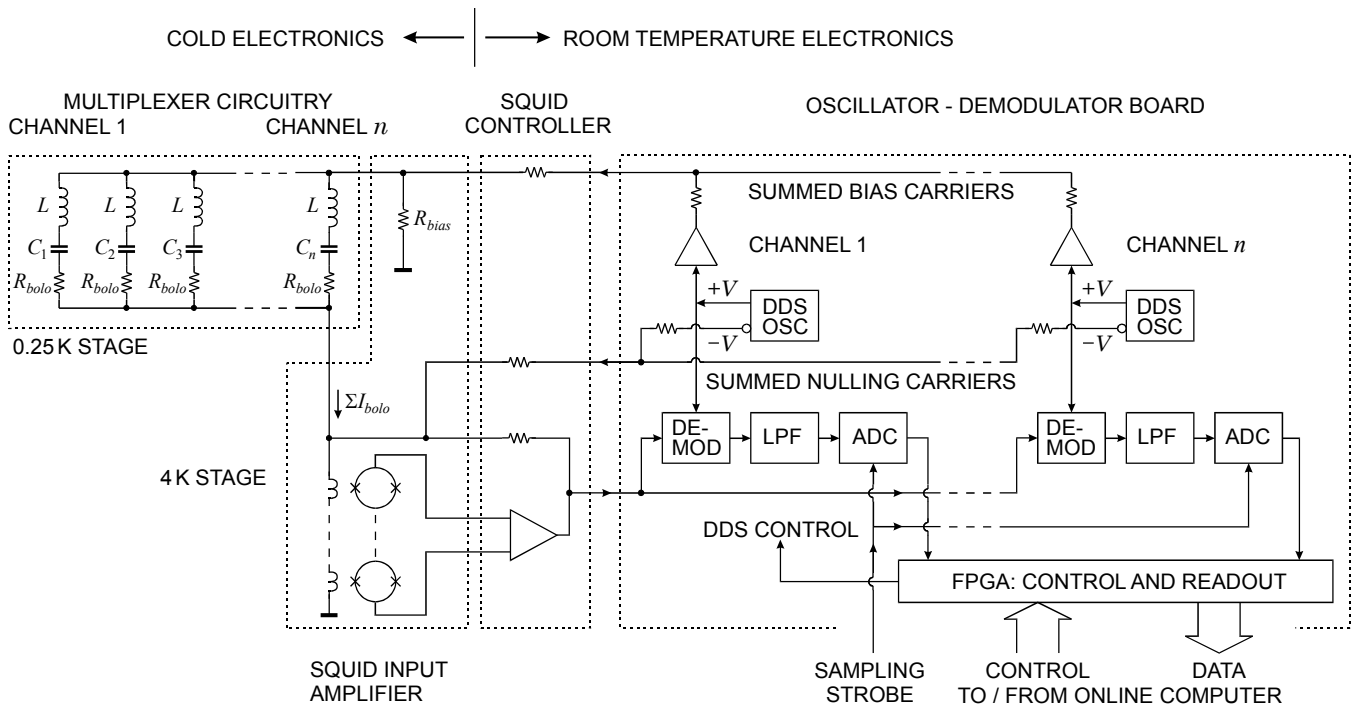


FIG. 2: Block diagram showing the basic topology of the fMUX readout system implementation, with an emphasis on the room temperature electronics. Refer to §IV for a description.

that spoil voltage bias or create cross-talk; avoiding detector oscillations which can affect other detectors in the same readout module through SQUID interactions; and, since the SQUID FLL includes a room temperature amplifier, achieving loop stability in the present implementation of this transimpedance amplifier is contingent on short wire lengths between 4 K and room temperature.

C. Design Requirements

The TES detector properties, our telescope scan strategy, and our science goals define the following requirements for the fMUX readout system:

Noise: The noise contribution from the readout system should be small compared to photon and detector noise which is typically about $50 \text{ aW}/\sqrt{\text{Hz}}$ for ground-based mm-wavelength observations. The readout system receives noise contributions from its SQUID and room-temperature electronics amplifier stages, Johnson noise from the TES resistance, and Johnson noise leakage through the LCR_{bolo} filter from neighboring detector channels.

Detector Stability: The analog circuit that includes the TES must be stable across the full range of observation conditions.

Cross-talk: Typical detector-to-detector cross-talk for our systems due to beam side-lobes and radiation leakage in the bolometer integration cavity is $\sim 1\%$. The readout system electrical cross-talk should be small in

comparison.

Dynamic Range: The readout system amplification needs to have sufficient dynamic range to accommodate the large bias carriers without introducing significant intermodulation distortion. The dynamic range requirement is substantially reduced for the fMUX system by canceling the carriers at the SQUID input with nulling signals that are inverted versions of the raw bias carriers, described in §IV.

Bandwidth and Post-Detection Sampling Rate: The telescope scan strategy defines a low frequency stability requirement of better than $\sim 1 \text{ Hz}$ which places stringent stability requirements on the sideband noise of the bias carriers. The fastest expected thermalization time constant of the detector absorber, $\tau_{\text{web}} \simeq 5 \text{ ms}$ (often referred to as the “optical time constant”), defines 30 Hz as the upper end of the signal band. Note that much higher bandwidths are of interest for characterizing bolometers, since the response time of the TES thermistor $\tau_{\text{TES}}^{\text{eff}}$ can be much faster than the bolometer optical time constant. This motivates a sampling rate in the range of 100-1000 Hz. Refer to Table I for definitions of the time constants used in this paper and Ref. [53] for a detailed thermal description of the detectors, including time response and diagrams.

Programmability: The system needs to operate autonomously under computer control, tuning and setting up each SQUID and detector. This tuning needs to be dynamic, so that changes in operating conditions (such as small changes in cryogenic temperatures or large changes

τ_{web}	thermalization time constant of the detector radiation absorber
τ_{TES}^{eff}	effective TES response time for thermal signals
τ_{LCR}	electrical time constant of the notch filter formed by the bolometer resistance and multiplexer inductor/capacitor

TABLE I: Definitions for the time constants utilized in this paper.

in atmospheric loading) do not adversely affect the system yield or operation.

Diagnostics: The system must provide sufficient diagnostic information so as to characterize detector performance, recognize problems such as failed tunings, and provide feedback to the telescope operator.

III. SUB-KELVIN MULTIPLEXER

One of the advantages for the fMUX system is the simplicity of the sub-kelvin readout components, consisting only of capacitors, inductors, and wiring. However, as discussed in this section, successful implementation of an fMUX system requires careful management of stray reactances to maintain good detector stability and optimal system noise. In addition to describing the specific implementations of the sub-kelvin multiplexer components for APEX-SZ and SPT in this section, after first describing the TES bolometers, we outline the design process that leads to the choice of parameters.

A. TES Bolometer Arrays

The APEX-SZ and SPT TES bolometer arrays (Figure 3,) were fabricated at UC Berkeley [54–56]. The detector arrays consist of six triangular shaped wedges, which together form a hexagonal array of 330 and 966 bolometers respectively for APEX-SZ and SPT. Short sections of circular wave-guide with conical feed-horns define the lower edge of the detector band and couple the detectors to free space. Metal mesh filters [57, 58] located above the feed-horns define the upper band edge. The bolometers are electrically connected to the cold multiplexer components with aluminum wire bonds on the periphery of the bolometer array.

The bolometers each consist of a 3 mm diameter gold absorber suspended above the 0.26 K cold stage bath through a thermal conductance in the range of $\bar{G}=100\text{--}200\text{ pW/K}$, where the bar indicates \bar{G} is averaged across the temperature difference between the TES transition temperature and its thermal bath. The bolometer operates with total power $P_{total} = \bar{G}(T_{bolo} - T_{bath})$ flowing to the bath. Optimizing \bar{G} is a trade-off between (1) lower noise, which pushes \bar{G} to lower values, and (2) high dynamic range for observations at a variety of optical loading conditions, which pushes \bar{G} to higher values. For APEX-SZ and SPT, the target \bar{G} has been

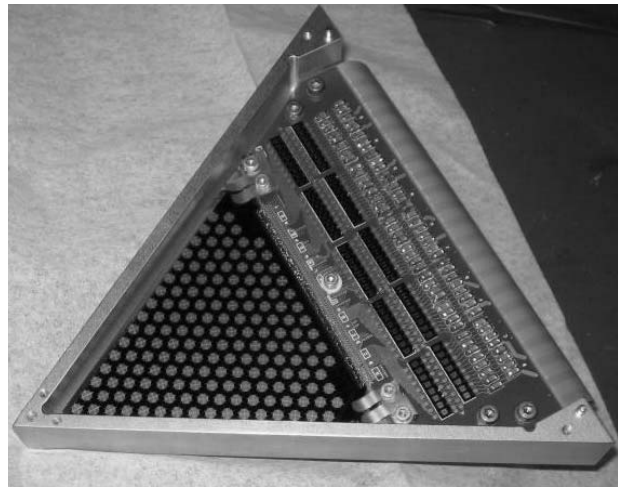


FIG. 3: Photograph showing one wedge of 161 SPT TES bolometers. The bolometer wedge is wire-bonded to a circuit board on which the multiplexer inductors and capacitors are mounted. An integrated flexible microstrip (visible at the right of the photo) brings the leads to connectors mounted below the circuit board. The band-defining feed-horns and metal mesh filters have been removed for this photo.

chosen so that the detector saturation power is slightly larger than twice the typical incident radiation power, $P_{total} \gtrsim 2 P_{rad}$, which maintains high electro-thermal loop-gain (discussed below) under all observing conditions.

The bolometer absorber has a spiderweb geometry, which provides a high optical efficiency while minimizing the cross section to cosmic rays. An Al/Ti bilayer TES is located at the center of each spiderweb and tuned to a superconducting transition temperature $T_{bolo} \sim 0.55\text{ K}$ and normal resistance $R_{normal} \sim 1.2\ \Omega$. The thermalization time of the spiderweb τ_{web} , typically 10–15 ms (16–11 Hz) for our detectors, sets the device’s response time for optical signals. The TES has a response time τ_{TES}^{eff} to thermal signals that is sped up by electro-thermal feedback and is typically more than an order of magnitude faster than τ_{web} . Since a fast τ_{TES}^{eff} places additional constraints on the readout system (see §III A 2), the TES time constant is slowed down by attaching a gold feature with considerable heat capacity [53]. Typical optical efficiencies (for the conversion of power from astronomical radiation to electrical power) are $\sim 80\%$ for light incident on the detectors, and about 20–40% end-to-end from the telescope’s primary dish. References [2] and [52] provide discussions of the APEX-SZ and SPT optical efficiencies respectively.

1. Detector Bias and Electro-Thermal Feedback

The TES are biased with a fixed amplitude sinusoidal voltage at frequencies much higher (faster) than the TES can respond, so it sees the integrated bias power. The

steep $\Delta R_{\text{bolo}}/\Delta T$ TES transition and voltage bias provide the conditions for strong negative electro-thermal feedback (ETF) [59]. When the radiation power P_{rad} incident on the bolometer increases, the bolometer temperature T_{bolo} increases, driving up its resistance R_{bolo} . This, in turn, brings down the electrical bias power $P_{\text{elec}}^{\omega^i} = V_{\text{bias}}^2/R_{\text{bolo}}$ provided by the sinusoid at frequency ω^i , completing the negative ETF loop.

ETF improves linearity, extends the dynamic range, and speeds up the effective TES response time for thermal signals. A measure of the ETF strength is the loop-gain,

$$\mathcal{L}_i = \frac{\alpha P_{\text{elec}}^{\omega^i}}{GT_{\text{bolo}}}, \quad (1)$$

where $\alpha = d\log(R_{\text{bolo}})/d\log(T_{\text{bolo}})$ is the logarithmic derivative of the bolometer resistance R_{bolo} with temperature T_{bolo} , $G = dP_{\text{total}}/dT_{\text{bolo}}$ is the instantaneous thermal conductance between the bolometer absorber and bath, and T_{bolo} is the TES transition temperature. When the loop-gain is high, the total power on the bolometer $P_{\text{total}} = P_{\text{rad}} + P_{\text{elec}}^{\omega^i}$ will be approximately constant and balanced by the rate of heat transmitted to the bath, $P_{\text{total}} = \bar{G}(T_{\text{bolo}} - T_{\text{bath}}) = \int_{T_{\text{bath}}}^{T_{\text{bolo}}} GdT$.

One simple strategy for providing voltage bias is to place the TES in a loop with a small bias resistor, $R_{\text{bias}} \ll R_{\text{bolo}}$ shown in Figure 1, across which the voltage bias is provided by an external current source. This loop consists of the bias resistor, one bolometer, the inductor and capacitor that define the loop resonant frequency, and the transimpedance amplifier input. Ideally, all other components in the loop would have negligible impedance in comparison with the bolometer. This includes the transimpedance amplifier that measures the TES current, wiring, and any other components such as the inductors and capacitors that define the resonant frequency. The wiring that connects the bolometers on the sub-kelvin stage to the low impedance ammeter (in this implementation, a SQUID array located on a 4K stage) can be substantial in length and span large temperature gradients. Wiring resistance can be kept low while maintaining low thermal-conductivity by constructing the wires from a superconductor, such as NbTi. Since this wiring lies outside the tuned LCR_{bolo} leg of the loop, its inductance L can not be tuned out by the fMUX capacitor for more than one channel. This means it is necessary to keep the wiring inductance low enough that the reactance is small compared to R_{bolo} at the resonant frequency. Meeting this requirement is difficult with traditional twisted pair wiring (50 nH amounts to $0.3j\Omega$ at 1 MHz, where j denotes the imaginary component), so that low inductance microstrips are necessary for all or part of this wiring (see §IV D).

2. Bandwidth and Detector Stability

To avoid under-damped or exponentially growing oscillations in the TES response, the electrical power (half-width at half maximum, HWHM) bandwidth of the LCR_{bolo} filter $1/\tau_{\text{LCR}}$ must exceed the TES thermal bandwidth $1/\tau_{\text{TES}}^{\text{eff}}$ by a factor $1/\tau_{\text{LCR}} \geq 5.8/\tau_{\text{TES}}^{\text{eff}}$ [60] (see Ref. [61] for a thorough description). For the APEX-SZ and SPT detectors with $R_{\text{bolo}} \simeq 1\Omega$ and thermalisation time constant $\tau_{\text{web}} \geq 5\text{ms}$ (32 Hz roll-off frequency), we employ 15.8 μH inductors to maximize the detector readout bandwidth while still meeting our constraint on cross-channel current leakage. This results in the requirement $\tau_{\text{TES}}^{\text{eff}} > 0.2\text{ms}$ (0.8 kHz roll-off frequency). This allows for an order of magnitude range ($0.2\text{ms} < \tau_{\text{TES}}^{\text{eff}} < 5\text{ms}$) for the TES time constant. The TES time constants are increased to lie within this range by adding a heat capacity in the form of an Au island that has a strong thermal coupling to the TES. However, since the $\tau_{\text{TES}}^{\text{eff}}$ is sped up by the loop-gain of the ETF, it is important to have a substantial stability range. This stability requirement defines the minimum allowed LCR_{bolo} bandwidth, and hence the channel spacing (described below) for the fMUX system.

B. Multiplexer Channel Spacing

The spacing between adjacent multiplexer channels is chosen such that (1) Johnson noise leakage from adjacent channels is small, (2) bias current leakage from adjacent channels does not spoil the detector voltage bias, and (3) cross-talk between neighboring detectors on a comb is small in comparison to the other sources of cross-talk in the experiment. These conditions must hold for the LCR_{bolo} bandwidth that is defined by the ETF stability requirements discussed in §III A 2. For APEX-SZ and SPT a channel spacing of 75 kHz is used. The first two criteria are discussed below, while cross-talk is discussed in §III C.

Each bolometer in the multiplexer module is a source of broadband Johnson noise. The SQUID input receives the sum of all Johnson noise contributions from every channel, so it is necessary to space the channels far enough apart in frequency so that the Johnson noise from neighboring channels is attenuated to a negligible level. This requirement is not the dominant constraint for channel spacing. At a frequency of 75 kHz away from resonance, for $L = 15.8\mu\text{H}$ and $R_{\text{bolo}} = 1\Omega$, the Johnson noise current of a detector is attenuated by a factor 15, providing an increase of just 0.2% to the total Johnson current noise of its neighbor. The increase in total detector noise is substantially smaller than this when other noise sources are also considered. The Johnson noise leakage from spacings as close as 4 times the LCR_{bolo} bandwidth (20 kHz, in this case) or less could be tolerated, contributing a 3% increase in the Johnson noise current of a neighbor.

A more serious constraint on channel spacing is bias current leakage. In addition to its own on-resonance bias, bolometer channel i also sees a fraction of the current from the $i \pm 1$ nearest carriers that neighbor in frequency space. The magnitude ratio of the off-resonance current $I_{\text{Ch } i}^{\omega_{i \pm 1}}$ from the neighboring carrier bias to the on-resonance current $I_{\text{Ch } i}^{\omega_i}$ flowing through bolometer channel i is

$$\frac{I_{\text{Ch } i}^{\omega_{i \pm 1}}}{I_{\text{Ch } i}^{\omega_i}} = \frac{R_{\text{bolo}}}{\sqrt{R_{\text{bolo}}^2 + (\omega_{i \pm 1} L - \frac{1}{\omega_{i \pm 1} C_{\text{Ch } i}})^2}}, \quad (2)$$

where R_{bolo} is the bolometer resistance, L is the series inductor, $C_{\text{Ch } i}$ is the series capacitor, and $\omega_{i \pm 1}$ is the angular frequency of the adjacent bias carrier. For the channel spacing and parameters considered here, this may be approximated $I_{\text{Ch } i}^{\omega_{i \pm 1}} / I_{\text{Ch } i}^{\omega_i} \approx \frac{R_{\text{bolo}}}{2\Delta\omega L}$, where $\Delta\omega$ is the channel spacing.

Bias carrier leakage can be problematic, mostly because of cross-talk (discussed below), but also because the leakage is a quasi-current bias that provides a positive ETF contribution to the total bias power seen by the bolometer. While the negative ETF afforded by the on-resonance voltage bias will dominate, the contribution from carrier leakage can cause instability and will also enhance the bolometer responsivity slightly.

All of these effects are rather small in practice. For a spacing of 50 kHz (10 times the LCR_{bolo} bandwidth), the electrical bias power from one of the nearest neighbors is roughly 1% of the on-resonance power assuming that all bolometers are biased at the same voltage amplitude. For channels biased near the center of the bias-frequency comb, the total off-resonance bias power is approximately 3%. This leads to a 3% increase in both the responsivity and the effective time constant, and a 3% decrease in the maximum loopgain. At our spacing of 75 kHz (15 times the LCR_{bolo} bandwidth), these effects are reduced to 1%.

C. Cross-talk

The multiplexer contributes channel-to-channel cross-talk due to (1) inductor cross-coupling, (2) bias carrier leakage, and (3) signals from a detector causing heating in neighbor detectors due to the voltage drop across non-zero SQUID or wiring impedance. Contributions from these mechanisms, discussed below, are smaller than the $\sim 1\%$ optical cross-talk that typically exists between neighboring pixels for APEX-SZ and SPT.

(1) Inductor cross-coupling: The mutual inductance $M_{i,j} = k_{i,j} L_i L_j$ between inductors L_i and L_j of two channels i and j in a multiplexer module creates cross-talk. The carrier current I_i flowing through the i^{th} bolometer channel induces a voltage $|V_j| = \omega_i M_{i,j} I_i$ in the inductor j that physically neighbors channel i . As R_{bolo}^i changes in response to sky signals, the voltage V_j is modulated as well. This modulation produces small changes in the current flowing in channel j since R_{bolo}^j

forms a small fraction of the total LCR_{bolo}^j impedance at frequencies far from its resonance. The measured coupling coefficient [25] between neighboring inductors on the same chip is $k = 0.010 \pm 0.002$ for the fMUX system. This form of cross-talk can be made negligible by ensuring that channels with physically neighboring inductors are not neighbors in frequency space (i.e., that physically neighboring inductors in this implementation have carrier bias frequencies separated by more than 150 kHz).

(2) Bias carrier leakage: As R_{bolo} changes in response to sky signals incident on bolometer i , both its on-resonance carrier at frequency ω_i and the off-resonance leakage bias carriers at neighboring frequencies $\omega_{i \pm 1}$ are modulated, creating cross-talk. This mechanism encodes a cross-talk sky-signal on the leakage current waveform. The signal appears as an amplitude modulation in the on-resonance carrier, but leads to modulation in both the amplitude and the phase of the off-resonance carrier. Thus a full quadrature demodulator would see cross talk signal in both the I- and Q-components of the demodulator output. However, the demodulator measures only the I-component modulations. For an off-resonance LCR_{bolo} channel $i \pm 1$ at carrier frequency ω_i , the amplitude fluctuation is:

$$I_{\text{Ch } i \pm 1}^{\omega_i} = \frac{V_{\text{bias}}^{\omega_i}}{R_{\text{bolo}} + j\omega_i L + 1/(j\omega_i C_{\text{Ch } i \pm 1})} \quad (3)$$

$$\simeq \frac{V_{\text{bias}}^{\omega_i}}{R_{\text{bolo}} + j2\Delta\omega L} \quad (4)$$

$$\simeq \frac{V_{\text{bias}}^{\omega_i}}{j2\Delta\omega L} \left(1 + \frac{jR_{\text{bolo}}}{2\Delta\omega L} \right), \quad (5)$$

where a first-order Taylor expansion in the parameter $\frac{jR_{\text{bolo}}}{2\Delta\omega L}$ has been performed for the last equality. This results in a current modulation with a change in bolometer resistance of

$$\frac{\Delta I_{\text{Ch } i \pm 1}^{\omega_i}}{\Delta R_{\text{bolo}}} \simeq \frac{V_{\text{bias}}^{\omega_i}}{(2\Delta\omega L)^2}, \quad (6)$$

which should be compared to the current modulation

$$\frac{\Delta I_{\text{Ch } i}^{\omega_i}}{\Delta R_{\text{bolo}}} \simeq \frac{-V_{\text{bias}}^{\omega_i}}{R_{\text{bolo}}^2} \quad (7)$$

that would occur on-resonance. The magnitude ratio of Equation 6 to Equation 7

$$\left| \frac{R_{\text{bolo}}^2}{(2\Delta\omega L)^2} \right| \quad (8)$$

is a good approximation for this cross-talk. This is equivalent to the square of the current leakage ratio presented in Equation 2. For our circuit parameters ($R_{\text{bolo}} = 0.75 \Omega$, $\Delta\omega = 2\pi \cdot 75 \text{ kHz}$, $L = 15.8 \mu\text{H}$), this effect results in $\sim 0.25\%$ cross-talk. Note that this is larger than the cross-talk estimate that was derived in Ref. [25], which did not correctly take into account the phase of this cross-talk signal.

(3) Non-zero SQUID/wiring impedance: A change in bolometer impedance of channel i in response to sky-signals, causes the voltage at carrier frequency ω_i across the stray SQUID and wiring reactance to be modulated, which in turn causes a modulation in the leakage current power deposited in neighboring detectors $i \pm 1$. This mechanism transmits cross-talk power from the on-resonance detector to the off-resonance neighbors, which is the opposite transfer direction compared to mechanism (2). The voltage V_{module} across the sub-kelvin multiplexer module (measured from the right side of p1 to the right side of p2 in Figure 4) is not exactly equal to the voltage V_{bias} across the bias resistor. This discrepancy arises from the non-zero complex input impedance of the SQUID system (p5 in Figure 4) and the stray inductance of the wiring (p1 and p2 in Figure 4) that connects the module to the SQUID input (together labelled V_{stray}) such that $V_{\text{module}} = V_{\text{bias}} - V_{\text{stray}}$. For the purposes of this discussion, the p3 and p4 stray components in Figure 4 can be ignored. Consider the current $I_{\text{Ch } i}^{\omega_i}$ at carrier frequency ω_i that flows predominantly through the i^{th} bolometer. The change in voltage across the module due to a change $dI_{\text{Ch } i}^{\omega_i}$ is

$$dV_{\text{module}} = dV_{\text{bias}} - dV_{\text{stray}} \quad (9)$$

$$= -dV_{\text{stray}} = -dI_{\text{Ch } i}^{\omega_i} Z_{\text{stray}} \quad (10)$$

$$\simeq -dI_{\text{Ch } i}^{\omega_i} \cdot j\omega_i L_{\text{stray}} \quad (11)$$

at fixed V_{bias} . We have assumed that the SQUID system and wiring impedances Z_{stray} are dominated by an inductive term L_{stray} . This voltage induces a leakage current $dI_{\text{Ch } i \pm 1}^{\omega_i}$ through the neighboring $i \pm 1$ bolometer channel

$$dI_{\text{Ch } i \pm 1}^{\omega_i} = \frac{dV_{\text{module}}}{Z_{\text{Ch } i \pm 1}^{\text{LCR}}} \simeq \frac{-dI_{\text{Ch } i}^{\omega_i} \cdot j\omega_i L_{\text{stray}}}{j2\Delta\omega L}, \quad (12)$$

where $Z_{\text{Ch } i \pm 1}^{\text{LCR}} \simeq j2\Delta\omega L$ is the impedance of the neighboring $i \pm 1$ LCR_{bolo} leg of the cold multiplexer module at frequency ω_i . This current fluctuation deposits Joule heating power

$$dP_{\text{Ch } i \pm 1}^{\omega_i} \simeq 2R_{\text{bolo}} I_{\text{Ch } i \pm 1}^{\omega_i} \cdot dI_{\text{Ch } i \pm 1}^{\omega_i} \quad (13)$$

in the neighboring bolometer channel, which should be compared to the signal in Channel i ,

$$dP_{\text{Ch } i}^{\omega_i} \simeq dI_{\text{Ch } i}^{\omega_i} V_{\text{module}}. \quad (14)$$

The ratio of these power fluctuations is the cross talk,

$$\frac{dP_{\text{Ch } i \pm 1}^{\omega_i}}{dP_{\text{Ch } i}^{\omega_i}} \simeq -\frac{I_{\text{Ch } i \pm 1}^{\omega_i}}{I_{\text{Ch } i}^{\omega_i}} \frac{\omega_i}{\Delta\omega} \frac{L_{\text{stray}}}{L}. \quad (15)$$

For the fMUX system with $L/L_{\text{stray}} \sim 150$, $R_{\text{bolo}} = 0.75 \Omega$, $\Delta\omega = 2\pi \cdot 75 \text{ kHz}$, and taking $\omega_i = 2\pi \cdot 750 \text{ kHz}$, this cross-talk amounts to 0.3%.

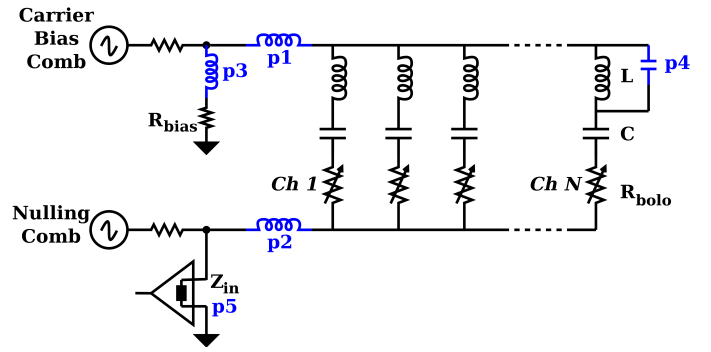


FIG. 4: Stray reactances in the sub-kelvin multiplexer circuit are problematic since the circuit operates at MHz frequency with characteristic impedances $\sim 1\Omega$. The stray inductance of the wiring connecting the bias resistor (R_{bias}) to the multiplexer circuit is shown at p1 and p2, the stray inductance in series with R_{bias} is shown at p3, the stray capacitance in parallel with a channel's inductor is shown at p4, and the non-zero input impedance of the transimpedance pre-amplifier is shown at p5.

While the three forms of readout system cross-talk discussed above would not be present in a non-multiplexed system, we note that a dominant form of electronic cross-talk for a non-multiplexed system can be eliminated for the fMUX system. Capacitive coupling of wires within multi-wire cables that carry signals from different detector channels is typically $\sim 1\%$ for bundles of twisted pairs. For a non-multiplexed system, all detector signals normally occupy the same frequency bandwidth as they are transmitted through these cables, resulting in 1% cross talk with neighbors. For the fMUX system, each wire carries a module of detectors, each at a unique bias frequency. Since the $\sim 100 \text{ Hz}$ signal bandwidth is a small fraction of the total bandwidth, the bias frequencies of modules that are bundled together can be chosen to be unique. This places the cable cross-talk signals in a portion of the bandwidth that is discarded by the signal demodulation. This means that, overall, this multiplexed readout system has lower cross-talk than a typical non-multiplexed system.

D. Channel Count

Considering the results of the previous sections, the number of channels that can be multiplexed together without adversely affecting the noise or cross-talk for a system with a given set of parameters is derived as follows.

The LCR_{bolo} HWHM power bandwidth is chosen to be at least 5.8 times wider than the inverse of the fastest expected TES time constant, $1/(2\pi\tau_{\text{TES}}^{\text{eff}})$ (see § III A 2). This has very conservatively been chosen to be 5 kHz in this system, allowing an order of magnitude range of $0.2 \text{ ms} < \tau_{\text{TES}}^{\text{eff}} < 5 \text{ ms}$ so that the time constants are ordered appropriately as $5.8 \tau_{\text{LCR}} < \tau_{\text{TES}}^{\text{eff}} < \tau_{\text{web}}$.

The spacing between LCR_{bolo} resonances is chosen so that the total bias carrier leakage current is less than 20% of the on-resonance carrier current, and the cross-talk is less than 0.5%. For the parameters of this system, this results in a spacing of 15 times the LCR_{bolo} bandwidth, 75 kHz. This spacing also keeps Johnson noise leakage at a negligible level.

Having specified the channel spacing, the number of channels is defined by the bandwidth of the low impedance amplifier. The SQUID shunt-feedback circuit (discussed in §IV B) for this system has a bandwidth of 1 MHz. The carriers are positioned between about 400 kHz and 900 kHz, ensuring odd harmonics from low-frequency carriers do not fall within the bandwidth of higher frequency channels. Odd harmonics are the dominant form of distortion from SQUID non-linearity. Bias carriers below 400 kHz are avoided because of the difficulty of finding high-Q capacitors with sufficiently high capacitance that behave well at cryogenic temperatures. These considerations result in 7 channels per multiplexer module so that the number of wires connecting the sub-kelvin multiplexer to the 4 K SQUID is the total number of detectors multiplied by 2/7.

The per-module channel count for APEX-SZ and SPT is conservative. A small increase in channel count could be achieved by slowing the TES time constants $\tau_{\text{TES}}^{\text{eff}}$ so that they are better matched to the absorber thermalization time τ_{web} , allowing narrower channel spacing. Substantial increases could be achieved by implementing a SQUID flux-locked loop (FLL) with substantially larger bandwidth such as Ref. [62]. Finally, much narrower channel spacing could be realized by using a sharper band-pass filter than the single pole LCR_{bolo} employed here, although this would substantially complicate the cold circuit.

E. Sub-kelvin Multiplexer Implementation

Each sub-kelvin multiplexer module consists of a custom-fabricated chip of seven inductors, seven commercially available ceramic capacitors with negative-positive-zero (NP0) dielectric material, and a custom printed circuit board (shared by all multiplexer modules for a particular detector wafer) on which these components are mounted. The multiplexer modules are interfaced with aluminum wire bonds to the detector wafer as shown in Figure 3. The circuit board is thermally sunk to the same 250 mK temperature stage as the bolometers.

The inductors were custom fabricated at the Northrop-Grumman superconducting micro-fabrication facility with a lithographic process. Each chip consists of eight inductors, of which we use seven. One inductor is about $1.5 \text{ mm} \times 1.5 \text{ mm}$, consisting of a 140 turn spiral ($2 \mu\text{m}$ width niobium trace with pitch of $4 \mu\text{m}$) separated by a 50 nm SiO_2 insulating layer from a niobium, flux-focusing washer that is left floating. The $15.8 \mu\text{H}$ inductance is the same for all channels in the module. The Northrop-

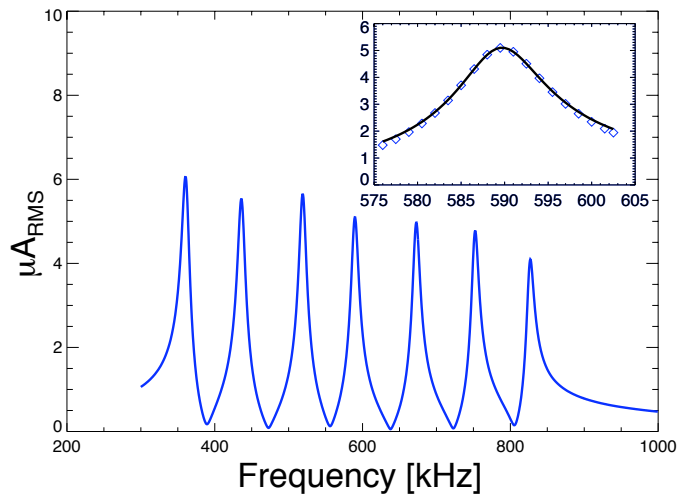


FIG. 5: The resonant frequencies for each LCR_{bolo} leg of the multiplexer circuit are measured by frequency-sweeping a small amplitude bias carrier across the range of carrier frequencies with the bolometer stage temperature held just above the detector superconducting transition. The resultant network analysis data, shown in the amplitude vs. frequency plot above, is fitted with a model to determine the optimum carrier bias frequency for each bolometer. One such fit is shown in the inset.

Grumman superconducting microlab is no longer available, and inductors for new implementations of the fMUX system are now being fabricated at the National Institute for Standards and Technology (NIST).

The frequency of each channel resonance is set by the series capacitor, for which we use commercially available surface mount capacitors. Our target spacing for the 7-channel multiplexer is 75 kHz. Several capacitors, pre-selected by measuring their capacitances individually, are stacked in parallel to achieve the target capacitance for each channel. The capacitances change by several percent when cooled from room temperature to 0.25 K, but in general all devices shift proportionately and the channel spacing is sufficiently preserved.

The resonant frequencies for each multiplexer module are measured by frequency-sweeping a small amplitude bias carrier across the range of carrier frequencies with the bolometer stage temperature held just above the detector superconducting transition. The amplitude of the current through the SQUID is measured. A representative ‘network analysis’ amplitude vs. frequency plot for a multiplexer module is shown in Figure 5. Each peak represents one bolometer channel, with its location, width, and height defined by the LCR_{bolo} parameters. The bias frequency for each bolometer is determined by fitting a model to each peak that includes parameters to account for the current flowing through off-resonant LCR_{bolo} legs in the multiplexer module.

F. Effects of Stray Reactances

Although the sub-kelvin multiplexer components are relatively simple, non-idealities in the form of stray inductances and capacitances can be problematic, since the circuit operates at MHz frequencies with characteristic impedances of about an ohm. The effect of these strays are discussed below.

The inductance of the cryogenic wiring that connects the bias resistor (R_{bias}) at 4 K to the sub-kelvin LCR_{bolo} multiplexer circuit is the most important stray, shown at p1 and p2 in Figure 4. This inductance is outside each LCR_{bolo} resonant circuit, and so cannot be tuned out at all of the carrier resonant frequencies. The voltage drop across this reactance reduces the voltage across the bolometer and partially spoils the constant voltage bias that is necessary for electro-thermal feedback. The effect is worse at higher frequency. To control this stray component, the wiring is constructed of two segments: a low inductance (~ 0.3 nH/cm) broadside coupled stripline is used for the majority of the wiring distance, followed by a short segment of NbTi twisted pair (~ 7 nH/cm) that is necessary to create a low thermal conductivity gap between the two temperature stages. The total inductance for this wiring in the system implementation is about 105 nH, amounting to $(0.2\text{-}0.6)j\Omega$ at 300-900 kHz, increasing the impedance of the on-resonance 0.75Ω bolometer circuit ($R_{\text{bolo}} + j\omega L_{\text{stray}}$) by 3-27%.

There is also a much smaller stray inductance in series with R_{bias} (p3 in Figure 4) that has the opposite effect compared to the above, increasing the bias voltage across the bolometer. The circuit board housing the SQUIDS and 30 m Ω bias resistors has been optimized to minimize this stray, which is estimated at ~ 4 nH. The total $R_{\text{bias}} + j\omega L_{\text{stray}}$ reactance increases from 31 m Ω at 300 kHz to 38 m Ω at 900 kHz. While this stray results in a large change (as much as 26% at 900 kHz) in the effective bias voltage across the bolometer, this phase and amplitude modified voltage still provides an effective bias for the purposes of ETF. To see this, we note that it would be possible to bias the bolometer using just an inductance in place of the bias resistor, eliminating Johnson noise from this component. The drawback is that the strong dependence on frequency of this inductance-bias voltage strategy would complicate the setup and tuning of the system. An inductive or capacitive voltage divider, as described in Ref. [50], would address both issues.

Both stray inductances described above affect the phase of the bias carriers in addition to their amplitude. Fortunately, the phase shifts of the two effects partially cancel. However, because of the lack of phase tuning capability for the demodulator in the backend electronics in this implementation of the readout (§IV C), this phase shift contributes to a slight degradation of noise at high frequency.

A stray capacitance is in parallel with the inductor (p4 in Figure 4) that forms the LCR_{bolo} series resonance for each multiplexer channel. This is due to a flux-focusing

washer below the spiral trace of each inductor. With the present architecture, the resonance is in the 16 MHz range. While this feature is well above the multiplexer bandwidth, the phase shift it produces can cause stability problems for the SQUID pre-amplifier feedback, discussed in §IV B.

The transimpedance pre-amplifier (a SQUID array in this implementation) has non-zero input reactance (p5 in Figure 4). This means that currents injected along the nulling wire are split between two return paths: (1) the desired path through the pre-amplifier, and (2) through the bolometers. We refer to path (2) as “nuller leakage”. Like the carrier voltage across the bias resistor, this leakage also appears as a voltage across the bolometers, with the pre-amplifier reactance playing the role of a bias resistor. This effect is more pronounced at higher frequencies. When the nuller current phase and amplitude is adjusted so that the net (carrier and nuller) current through the pre-amplifier is zero, the nuller current will be an exact inverted copy of the current through the bolometer. The nuller current is adjusted in this manner when the bolometers are tuned, forming a ‘virtual ground’ at the pre-amplifier input so that the net voltage across the input is zero after each tuning. Changes in observation loading conditions between bolometer tunings will result in a non-zero voltage across the pre-amplifier and alter the voltage bias across the bolometer.

Achieving the design requirements outlined in § II C has required careful handling of the stray components described above. Future readout systems that employ higher frequency carriers to multiplex a larger number of bolometer channels will need more advanced techniques to correct for these stray components.

IV. SQUID PRE-AMPLIFIER AND ROOM TEMPERATURE ELECTRONICS

Having described the design considerations for the sub-kelvin components in the previous section, we now describe the SQUID control and backend electronics in this section, beginning with the generation of the carriers that bias the detectors, then describing the SQUID pre-amplifier and its room temperature control electronics, and ending with the demodulation electronics.

The topology of the system is shown in Figure 2 for one 7-channel fMUX module. APEX-SZ uses 40 fMUX modules and SPT uses 120. Seven bias carriers are synthesized separately using Direct Digital Synthesizers (DDS) located on room temperature oscillator/demodulator boards. These analog carriers are added together to form a bias ‘comb’ and transmitted via a twisted pair cable and the room temperature SQUID controller board to the cryostat, where a 30 m Ω bias resistor at 4 K produces a voltage bias across the bolometers operating at 250 mK. LC resonant filters in series with the bolometers select a single carrier tone for each bolometer. Changes in optical power on the de-

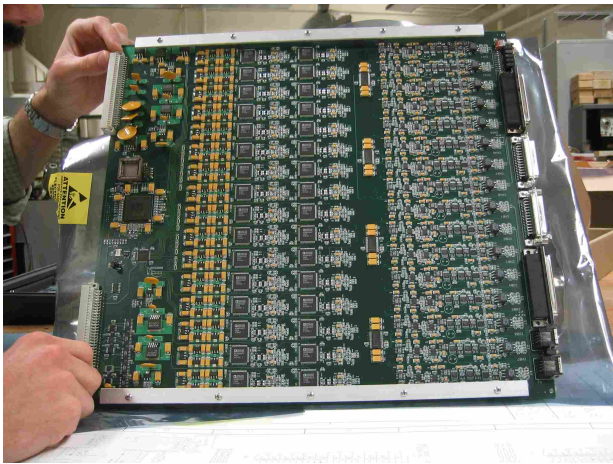


FIG. 6: (Color online) Photo showing the oscillator/demodulator circuit board that provides the biases and demodulates the outputs for 14 bolometer channels.

tectors induce amplitude modulation of the carrier currents which are summed together and pass through the input of a series-array SQUID device. The SQUID is coupled to a room temperature operational amplifier to form a shunt-feedback flux-locked-loop circuit. A separate ‘nulling comb’, which is simply an inverted version of the carrier comb, is transmitted from the oscillator/demodulator boards to the SQUID input. This serves to cancel the large carriers, reducing the dynamic range requirement for the SQUID. The nulled and amplified comb is transmitted via a cable to a bank of seven demodulators located on the oscillator/demodulator boards. Each amplitude-modulated carrier is demodulated separately, low-pass filtered, and digitized. The digitized sky-signals are transmitted to a data acquisition computer and recorded on disk. Each of these components is described in detail below.

A. Carrier Generation

The bolometer bias carriers are synthesized on custom circuit boards (Figure 6) that each handle 14 bolometer channels. In addition to synthesizing the carriers, these boards also perform the demodulation and digitization of the bolometer outputs described in §IV C. The layout of these boards is optimized to minimize cross-talk between channels and pickup from other electronics systems. A block diagram showing the circuit used to generate the carrier comb and nuller comb is shown in Figure 7.

The bias for each bolometer is generated with a Direct Digital Synthesizer (DDS, Analog Devices AD9854) that produces a sine wave by storing the waveform instantaneous phase in an accumulator and incrementing this accumulator every clock cycle. It uses the phase to address a corresponding amplitude in a look-up table, and sends that amplitude to a digital-to-analog con-

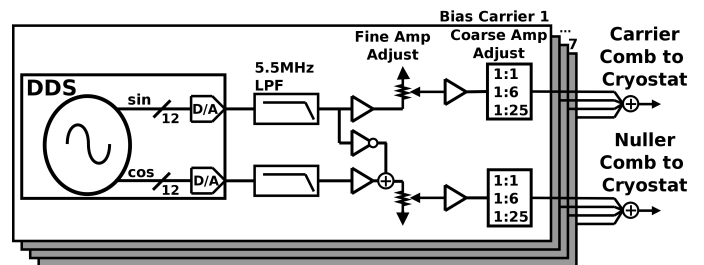


FIG. 7: Block diagram showing the carrier and nuller generation circuits. The sine and cosine outputs at the DDS have amplitude adjustment registers that are not shown. The DDS amplitudes are used to control the phase of the nuller signals by adjusting the admixtures of sine and cosine waves.

verter (DAC) sampling at 40 MHz. Because the phase information is held in only one register, it is not costly to achieve many bits of frequency resolution (these devices use a 48-bit phase accumulator and have μHz resolution). Having accurate amplitude information is more costly since each memory location within the look-up table needs this accuracy. Our devices provide 12-bit amplitude information. The output waveform can be multiplied pre-digitization by an amplitude adjustment factor that ranges from 0 to 1. In addition to the DAC providing the sine wave output, each DDS has a second DAC output that has a fixed 90 degree phase offset (i.e., a cosine wave) and separate amplitude adjustment factor. The DDS chips are the single biggest power consumers in the readout system, each one consuming $\sim 0.4\text{ W}$.

The DDS output signals are differential and each pass through low-pass 5.5 MHz analog filters to reduce clock bleed-through and limit the noise bandwidth of the bias carriers. The sine-wave output is used for the bolometer bias signals. An 8-bit digital potentiometer is used to control this amplitude. A coarse voltage attenuator can be enabled to provide further amplitude adjustment, allowing for good noise performance over a broad range of bolometer parameters. The analog differential output currents from eight oscillator circuits are summed together to produce a bias comb that is transmitted to the cryostat via a twisted pair cable and the SQUID controller boards. Seven of these eight outputs are used to bias the bolometers, the eighth is used as a test signal that can be injected one at a time to each of the bolometers in the comb.

The full scale carrier to white noise ratio is $\approx 6 \times 10^6 \sqrt{\text{Hz}}$, dominated by the digitization noise of the DDS. More important than the white noise level however, is the carrier sideband noise, since this noise eventually dominates at low frequencies and limits our ability to observe large angular scale signals on the sky. Carrier sideband noise can originate from clock jitter, DDS voltage reference jitter, and/or current noise in the transistors used in the DDS DAC. This system is not sensitive to clock-jitter, because the demodulator is driven by the same oscillator as the bias, approximately canceling the effect.

The dominant source of sideband noise is the low frequency noise of the DAC output transistors. This noise is proportional to the amplitude A_c of the carrier and measured to be $\sim A_c \times 10^{-5} / \sqrt{\text{Hz}}$ at 1 Hz away from the carrier, with a $1/f$ power spectrum.

In addition to the bias carrier generation, the same DDS circuits are used to provide the nulling signal that zeros the carrier amplitude just before the SQUID input. The nuller consists of an inverted version of the bias sine-wave, with a small admixture of the cosine signal from the second DDS output. The sum of these two signals is also a sine wave with a phase that can be programmed (by adjusting the cosine amplitude) from about 158 to 202 degrees from the bias carrier. This phase adjustment compensates for analog phase shifts between the carrier and nuller that arise because the two signals take different paths through the cold multiplexer (Figure 2). The filtering, amplitude adjustment, coarse attenuation, and summing circuits are the same for the nulling signals as for the carriers.

This scheme for synthesizing the nulling signal was motivated so that, when the cosine admixture is small, the bias low-frequency carrier sideband noise would be inverted for the nuller signal and subtract to zero at the input of the SQUID. This sideband-noise nulling was demonstrated to work very well when adding the carrier to the nuller through a resistor. However, the scheme does not work when used to bias bolometers, since the bolometer has an effective negative resistance within its active bandwidth. This means the sideband noise of the carrier is inverted by the bolometer, while its MHz carrier is not inverted. The net result is that the carrier sideband noise adds coherently to the nuller sideband noise. Though this results in excess low-frequency readout noise for this system, other sources of low-frequency noise dominate our detector noise (e.g., residual atmosphere, temperature drifts, etc.), and the low frequency noise from the readout does not dominate the overall low frequency noise of the experiment. The digital fMUX system described in Ref. [51]) uses a different scheme for nulling that avoids this excess readout noise.

B. SQUID Electronics

Transimpedance amplification of the bolometer currents is achieved with a series-array SQUID operating in a shunt-feedback circuit with a room temperature op-amp as shown in Figure 8. This circuit has the following properties: (1) Its input impedance is sufficiently low so as not to spoil the voltage bias across the bolometers. (2) It provides sufficient transimpedance so that the output signals can be interfaced to standard room-temperature amplifiers. (3) Its noise, referred to the input, is small compared to the bolometer noise. (4) It is sufficiently linear that intermodulation distortion is not an issue for the system operation.

For the fMUX system, the SQUIDs are housed in

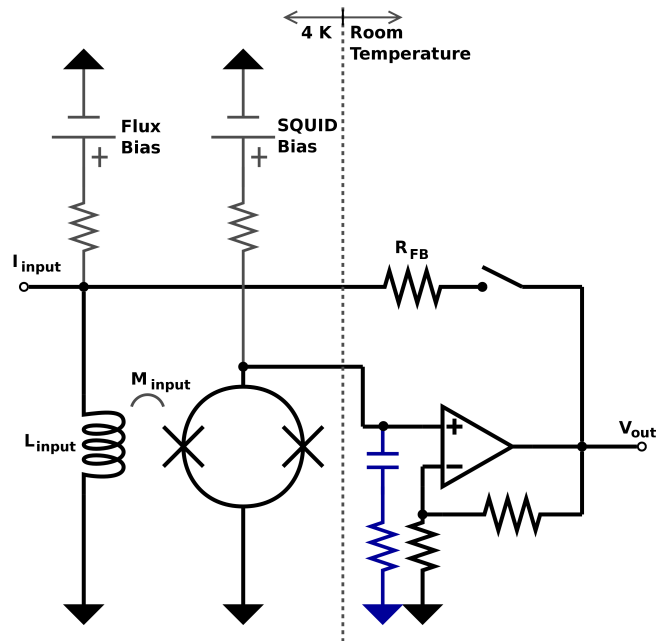


FIG. 8: The SQUID shunt-feedback circuit is shown. The capacitor and resistor that together form the lead-lag filter (refer to text) connect the non-inverting input of the operational amplifier to ground.

groups of eight on custom SQUID-mounting boards that are heat-sunk to the 4 K cryostat mainplate. The rest of the shunt-feedback circuit resides on custom room temperature SQUID-controller circuit boards, each of which manages eight SQUIDs. In addition to completing the shunt-feedback circuit, these electronics provide the bias currents for the SQUIDs and condition all analog signals entering the cryostat by attenuating them and filtering them for RF.

1. Series Array SQUID

Each bolometer module is connected directly to the input coil of a series-array SQUID manufactured at NIST [63]. Each array consists of 100 individual SQUID elements with their input coils, feedback coils, and outputs connected in series. The input signals add constructively while the output noise voltage of the individual elements adds incoherently, resulting in a signal-to-noise ratio that is enhanced by \sqrt{n} , where $n = 100$ is the number of elements. The array noise is $3.5 \text{ pA}/\sqrt{\text{Hz}}$ referred to the input coil and the bandwidth is 120 MHz.

Each SQUID element has two inductor coils that were intended for use separately as input coil and feedback coil. For shunt-feedback, the input coil is used for both functions. This coil array has an input inductance $L_{IN}^{SQ} \simeq 150 \text{ nH}$ and mutual inductance for each 8-turn element $M_{IN}^{SQ} \simeq 80 \text{ pH}$.

The response function for an open-loop SQUID may

be approximated as sinusoidal, with output voltage

$$V_{OUT}^{SQ} \simeq V_{PK} \sin(2\pi I_{IN}/I_{\Phi_0}), \quad (16)$$

where I_{IN} is the current through the input coil, V_{PK} is the peak output voltage of the device, and I_{Φ_0} is the input current required to provide a quantum of flux $\Phi_0 = h/2e$ through the SQUID. For our devices $I_{\Phi_0} \approx 25 \mu\text{A}$ and $V_{PK} \approx 1.5 - 3.5 \text{ mV}$ depending on fabrication reproducibility, operating temperature, and tuning. One can choose the operating point along the sinusoidal response curve using a static flux bias. For the shunt-feedback circuit, the devices are operated on the mid-point of the falling edge (see §IV B 5). The derivative of Equation 16 at this point is the transimpedance, $Z_{trans}^{SQ} \simeq -500\text{V/A}$, in good agreement with the measured performance of the devices.

2. Shunt-feedback Circuit

Shunt-feedback (Figure 8) is essential for linearizing the SQUID response and reducing the input reactance of the FLL circuit so that the bolometer impedance dominates the bias loop. Had the more common feedback configuration with separate feedback and input coils been used, it would increase the FLL circuit input impedance substantially, spoiling the bolometer voltage bias and relegating it to an unstable regime of electro-thermal feedback.

Shunt-feedback is rarely used for practical SQUID applications, because it couples the the strong input coil directly to the room temperature electronics, where pickup from digital components or RF signals are more difficult to shield against. Implementation of a shunt-feedback system requires careful filtering and shielding to prevent outside unwanted signals from reaching the SQUID input coil through the feedback line. Since this implementation is uncommon, the basic equations that characterize the shunt-feedback circuit operation are presented below.

An open-loop SQUID has input reactance $Z_{IN}^{SQ} \simeq j\omega L_{IN}^{SQ}$ (the reflected impedance of the SQUID is small at these frequencies and has been omitted), where ω is the angular frequency. The forward voltage gain of the open-loop SQUID/amplifier cascade is

$$\begin{aligned} G_{FWD} &= \frac{V_{OUT}^{AMP}}{V_{IN}^{SQ}} = \frac{-I_{IN}^{SQ} |Z_{trans}^{SQ} G^{AMP}|}{j I_{IN}^{SQ} \omega L_{IN}^{SQ}} \\ &= \frac{j |Z_{trans}^{SQ} G^{AMP}|}{\omega L_{IN}^{SQ}}, \end{aligned} \quad (17)$$

where V_{OUT}^{AMP} and V_{IN}^{SQ} are the voltages at the amplifier output and across the SQUID input coil respectively, I_{IN}^{SQ} is the current through the SQUID input coil, and $G^{AMP} \simeq 250$ is the non-inverting amplifier forward gain. The SQUID transimpedance is written

$Z_{trans}^{SQ} = -|Z_{trans}^{SQ}|$ to make explicit its operation in inverting mode. It is a simple extension to include the phase response of the amplifier.

When the switch in Figure 8 is closed to complete the feedback loop, input current is split between the SQUID coil and the feedback resistor, the latter of which has its impedance reduced by the forward gain of the circuit so that the total input impedance Z_{in}^{tot} is the parallel combination

$$Z_{in}^{tot} = Z_{IN}^{SQ} \parallel \frac{R_{FB}}{1 - G_{FWD}}. \quad (18)$$

For this system $G^{FWD} \gtrsim 10^5$ across a 1 MHz bandwidth and a computer controlled switch allows feedback resistors $R_{FB} = 3.3\text{k}\Omega$, $5\text{k}\Omega$, or $10\text{k}\Omega$ to be used. The circuit input impedance is 22-69 m Ω in the frequency range 300-900 kHz for the $R_{FB} = 10\text{k}\Omega$ feedback setting most commonly used for SPT and APEX-SZ.

The SQUID response function (Equation 16) defines its open-loop dynamic range as $I_{IN}^{\text{max, open loop}} = I_{\Phi_0}/2$. The shunt-feedback loop-gain

$$A_{loop}^{SQ} = \frac{-|Z_{trans}^{SQ}| \times G^{AMP}}{R_{FB}} \quad (19)$$

defines the extent to which the current through the SQUID coil is canceled by negative feedback, extending the SQUID dynamic range to

$$I_{IN}^{\text{max}} = \frac{I_{\Phi_0}}{2} \left(1 - \frac{2}{\pi} A_{loop}^{SQ} \right) \quad (20)$$

and vastly improving its linearity. For the fMUX implementation, $A_{loop}^{SQ} \simeq 38$, 25 , 12.5 for $R_{FB} = 3.3\text{k}\Omega$, $5\text{k}\Omega$, and $10\text{k}\Omega$ respectively. This results in a dynamic range that is extended by a factor 23, 15, and 7, respectively.

When the SQUID dynamic range is exceeded, the circuit ‘flux-jumps’ such that the SQUID is locked in a state one flux quantum or more away from its original locking point. This is similar to an operational amplifier hitting its rail and ‘sticking’ there. The FLL has drastically deteriorated dynamic range and linearity in its flux-jumped state. A flux-jump can be caused by electrical pick-up (typically of fast, digital signals), electrical glitches, or (very rarely) by a large magnitude electronic noise fluctuation.

For the 120 SQUID arrays in SPT, the flux-jumping rate is typically between 0 to 1 SQUID arrays per 24 hour observing cycle. There are several means of recovering from a flux-jump. The simplest method is to ‘reset’ the loop by either opening and closing it again (using the switch located in the feedback path, Figure 8) or removing and reinstating the SQUID bias. These ‘reset’ methods temporarily set the loop-gain A_{loop}^{SQ} to zero. This ‘reset’ only works if the input current through the SQUID coil is zero, otherwise the SQUID-loop will not be locked at the original locking point. A complication for this method is that, with $A_{loop}^{SQ} = 0$, the input impedance

Z_{in}^{tot} of the FLL is altered, which alters the resonant frequencies of the LCR_{bolo} resonant circuits. This can spoil ETF, causing the bolometer to oscillate and latch in a superconducting state. For the fMUX system, the SQUID input is always non-zero, due to sky-signal and imperfections in setting the nulling amplitude. Consequently, instead of ‘resetting’ the FLL, SQUID-jumps are recovered from by injecting a corrective current through the SQUID flux bias wire, and increasing this current until the SQUID jumps back to the original locking point.

3. Flux Locked Loop Stability

To maintain stability in the SQUID FLL circuit, phase shifts along the feedback loop must provide for negative feedback up to the frequency where the loop-gain bandwidth product falls below unity, 38 MHz for $R_{FB} = 3.3k\Omega$. The room temperature operational amplifier, with a bandwidth of 1 MHz, induces a 90° phase shift, allowing for an additional margin of 45° . This places stringent requirements on the length of the wires connecting the SQUIDs to the room temperature amplifier since a 0.66 m round-trip propagation delay amounts to 45° at 38 MHz. A one-way wiring length of 0.2 m is used for APEX-SZ and SPT. In the absence of phase shifts induced by strays, this lead length would allow stability. In practice, phase shifts arise from other non-idealities, such as the parallel resonance formed by the capacitive coupling of the MUX inductor to its flux-focusing washer or the wiring strays discussed in §III F.

To improve the FLL stability, a lead-lag filter is introduced and connects the output of the SQUID through a capacitor and resistor to ground, see Figure 8. At high frequency, this RC shunt-filter looks purely resistive and acts as a voltage divider with the SQUID output, attenuating the loop-gain. The filter introduces a phase shift at intermediate frequency, when the reactance of the capacitor is similar to the filter resistance. The filter capacitance is 1 nF and its resistance is set by a 0.2 m Manganin wire, about $15\ \Omega$. This filter introduces a frequency dependence on the SQUID transimpedance, attenuating it by about 30% at the high end (900 kHz) of the fMUX carrier bandwidth. It also introduces a phase shift inside the fMUX carrier bandwidth. These two effects contribute to a rise in the noise from the room temperature electronics at high bias carrier frequency, discussed in §V C.

4. SQUID Electronics Implementation

The SQUID electronics are implemented on two circuit boards: (1) a SQUID mounting board that houses the SQUIDs at 4 K and provides magnetic shielding, and (2) a room temperature SQUID Controller that houses the FLL operational amplifiers and SQUID bias current generation circuits, and conditions signals as they enter or exit the cryostat.

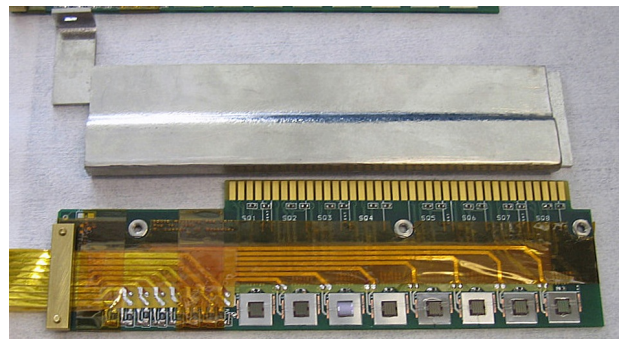


FIG. 9: (Color online) Photo showing the SQUID mounting board, housing eight NIST SQUID series arrays and the bias resistors for the bolometers. The SQUIDs are mounted on top of a Niobium film, visible in the photo. A magnetic shield enclosure, fabricated from the high magnetic permeability material Cryoperm, is shown above the circuit board.

The SQUID mounting boards, shown in Figure 9, are $0.15 \times 0.05\ \text{m}^2$ custom printed circuit boards housing eight SQUIDs each. SQUIDs are sensitive to changes in magnetic field, so that effective magnetic shielding is essential. Since the system employs series array SQUIDs, it is important to attenuate spatial variations as well as time variations in the magnetic field. This is because a spatial variation across the array would spoil the coherence of the individual SQUID elements.

Each SQUID is mounted with rubber cement on top of a $10 \times 10\ \text{mm}^2$ niobium film that is epoxied to the SQUID mounting board. Niobium is a Type II superconductor and serves to pin magnetic field lines, greatly attenuating their time variability. The entire circuit board is placed inside an enclosure built from a material that has a high magnetic permeability at cryogenic temperatures (Cryoperm, Vacuumschmelze GmbH, Grüner Weg 37 D-63450, Hanau, Germany). This attenuates the amplitude of the field lines, reducing both the temporal and spatial variability. The enclosure is open on two sides through narrow ‘‘chimneys’’ to allow wiring connections to the room temperature electronics through an edge connector, and to the cold multiplexer components through a broadside coupled stripline that is soldered directly to the board.

The $30\ \text{m}\Omega$ bolometer bias resistors (R_{bias} in Figure 2) are located on the SQUID mounting boards. This is a compromise, because the 4 K temperature means the bias resistors contribute about $2.5\ \text{pA}/\sqrt{\text{Hz}}$ of noise referred to the SQUID input. This would be reduced to a negligible level had this bias resistor been placed at 0.25 K with the sub-kelvin multiplexer components. By keeping the resistor at 4 K, we are able to connect to each multiplexer comb with just two wires instead of four, reducing the heat load on the sub-kelvin stage.

The SQUID controllers are $180 \times 170\ \text{mm}^2$ custom printed circuit boards. One board provides the control circuitry for eight SQUIDs. Each SQUID control circuit includes a high gain-bandwidth operational ampli-

fier with low ($1 \text{ nV}/\sqrt{\text{Hz}}$) input noise and two feedback resistors ($5\text{k}\Omega$ and $10\text{k}\Omega$, R_{FB} in Figure 8) that can be enabled individually or in parallel via software with an analog CMOS switch (adjacent to R_{FB} in Figure 8) that is selected for its low charge injection. A DAC provides four software programmable voltages for each SQUID that are used to (1) provide a current bias, about $150 \mu\text{A}$, through the SQUID, (2) provide a flux bias current, 0 - $25 \mu\text{A}$, to the SQUID input coil that is used to set the magnetic field through the SQUID, (3) zero the offset of the room temperature op-amp, and (4) provide a current to a heater resistor next to the SQUID that can be used to heat the SQUID above its superconducting transition.

Analog bolometer bias carrier signals and nulling signals are received from the oscillator/demodulator boards through isolation transformers on differential twisted pair cables, and attenuated on the SQUID controller board before being sent into the cryostat. The FLL output signals are transmitted from the SQUID controller boards to the oscillator/demodulator boards using differential drivers feeding twisted pair cables.

SQUIDs are very sensitive to digital pickup, so the digital circuitry on the SQUID controller boards is isolated from the analog circuitry by separating the local grounds and coupling the connections from the digital to analog circuitry through resistor-capacitor filters. Balanced connections between the SQUID controller and the demodulator circuit boards also suppress digital interference from the crate. Overall, digital noise pickup is negligible.

5. SQUID Setup and Tuning

The sorption fridge that cools the sub-kelvin stage of the system has a hold time of about 36 hours. Each time this fridge is cycled, the SQUIDs are tuned to configure them at their optimum operating point.

As the mainplate is cooled to 4 K, the SQUIDs cross their superconducting transition relatively slowly, with a thermal gradient across the series arrays. This gradient can transform time varying magnetic fields into spatially varying trapped flux across the series array. The first step in the tuning process is to raise the temperature of each SQUID by providing current to a heater resistor located next to it, bringing the device into the normal state and then allowing it to cool quickly, reducing the probability that time varying fields will be converted into spatially trapped flux.

The next step is to map out the SQUID output voltage response to a current through its input coil (approximated by Equation 16) as a function of the SQUID bias current, as shown in Figure 10. The bias current choice defines which of these “V-phi” curves the SQUID operates on.

The derivative of the V-phi curve is the SQUID transimpedance Z_{trans}^{SQ} . It defines the SQUID small signal response and is the quantity that refers the room temperature electronics noise back to an equivalent noise cur-

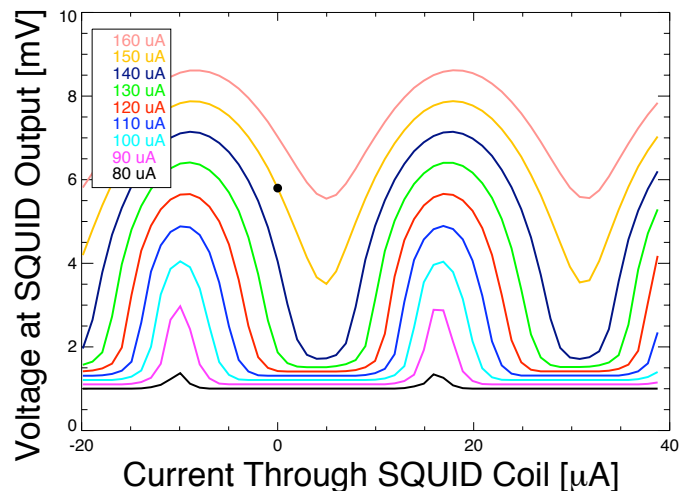


FIG. 10: (Color online) The SQUID voltage response to a linearly increasing current through the SQUID input coil (called a “V-phi” curve) is shown for several choices of the SQUID bias current ranging from $80 \mu\text{A}$ (bottom curve) to $160 \mu\text{A}$ (top curve). The chosen SQUID operating point is marked by a closed circle.

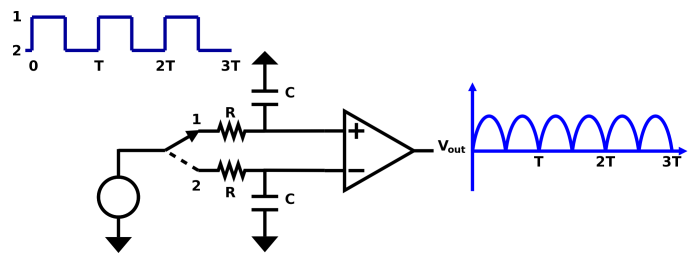


FIG. 11: Block diagram of the demodulator circuit.

rent through the bolometer. Ideally, Z_{trans}^{SQ} would be maximized. The peak-to-peak amplitude relates to the SQUID’s large signal response. The distance between peaks in each V-phi curve is the current required to produce a flux quantum through the SQUID coil, and is independent of the bias current. For stable SQUID operation, a smooth curve with a high level of symmetry around the chosen flux bias point is preferred. A typical choice for the SQUID operating point is indicated by the small red circle on the $150 \mu\text{A}$ SQUID bias curve (2nd from top). This represents a trade off between the criteria listed above.

Once the SQUID response has been mapped and the bias currents chosen, the feedback loop is closed so that the FLL is in its low input impedance state, allowing for bolometer operation.

C. Demodulator and Digitization

Each bolometer channel has its own analog demodulator that locks into the bias carrier and mixes the sky-

signal down to base-band. This demodulator is referenced with the same analog sine wave that biases its bolometer, serving to cancel the clock-jitter sideband noise. Sixteen demodulator channels are housed on each oscillator/demodulator board, as described in §IV A.

Eight demodulators (half of an oscillator/demodulator board) monitor each multiplexer module, consisting of seven bolometer channels. Seven of the demodulators are phase-locked to the in-phase I component of the seven bolometer carriers. The system was originally conceived with 8 bolometers per module, but this has been reduced to seven so that the eighth “helper” demodulator can be used periodically to measure the Q component (90 degrees out of phase) of each channel. Being able to simultaneously observe both I and Q components facilitates fast setup of the nulling signal amplitude and phase discussed in §IV E.

Each module of eight demodulators is AC coupled to the differential SQUID controller output through capacitors. An input transformer suppresses common-mode signals. In front of the coupling capacitors, a separate analog to digital converter (ADC) samples the SQUID static offset at 1 kHz, which is necessary for tuning the SQUIDS and monitoring for flux-jumps.

The signal from an individual bolometer is mixed down to base-band by multiplying it with a unit amplitude square wave. This is achieved (Figure 11) by passing the reference carrier sinusoid through a comparator and using its output to control an analog switch that acts as a synchronous rectifier on the input waveform. The output of this rectifier is sent to a pair of low-pass RC integrator circuits that remove the high frequency out-of-band signals produced by the other bolometer channels. The rectifier operates in a doubly-balanced mode, with differential input signals, not shown in Figure 11, as well as the differential output. This implementation is built up from discrete components and has excellent distortion performance because there are no non-linear elements. An instrumentation amplifier, with gain that is software selectable over two orders of magnitude, takes the difference between the two integrators. The preceding stages have sufficient gain to override the instrumentation amplifier’s low-frequency noise. The amplified base-band signal is anti-alias filtered with an 8-pole active low-pass filter operating at 400 Hz and digitized with a 12-bit ADC at 1 kHz.

A Field Programmable Gate Array (FPGA) on each oscillator/demodulator board assembles the outputs from the ADCs and sends the data via an 8-bit parallel low voltage differential signal (LVDS) connection to the readout control computer. A software low-pass filter with a 35 Hz pass-band is applied to the data, which is then down-sampled to 100 Hz and written to disk.

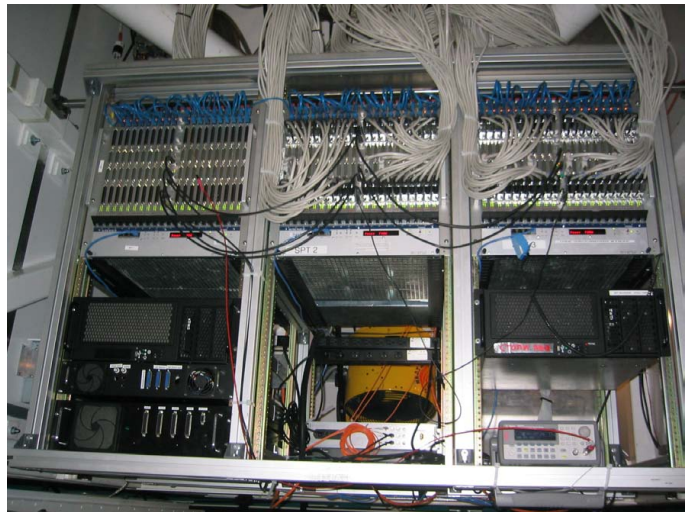


FIG. 12: (Color online) Photo showing the three readout electronics crates (top half of each rack) housing the oscillator/demodulator circuit boards in the cabin of the South Pole Telescope. Control computers, cryogenic housekeeping, timing, and network electronics are also visible in the bottom half of the racks.

D. Readout Electronics Crates, Interface, and Power Consumption

The 16-channel oscillator/demodulator circuit boards (Figure 6) are $340 \times 360 \text{ mm}^2$ in size and 20 circuit boards are packaged together in a 9U Versa Module Eurocard (VME) crate with custom backplanes that provide power to the boards and connect to the control computer. Each crate is convectively cooled with fans and has an integrated power supply. The power consumption is about 900 W per crate including the power delivered to the SQUID Controller electronics described above. Three crates (2700 W) house the oscillator/demodulator electronics for the 840 bolometer channels of SPT (photo Figure 12). The 280 channel APEX-SZ system requires one crate (900 W).

The center slot of each crate is used for a clock distribution circuit board that sends a central 40 MHz system clock and a once per second GPS-derived timestamp across the backplane to each oscillator/demodulator board. The system clock and timestamp signals can be daisy-chained across several clock distribution boards in different crates.

The system is interfaced to a control computer, running the Scientific Linux operating system. Command signals are received from the control computer through a single RS485 serial signal distributed across the backplane and encoded using the communications protocol Modbus (see <http://www.modbus.org>). Bolometer data, sampled at 1 kHz, flow from the readout crate backplanes to the control computer through an 8-bit parallel low voltage differential signal (LVDS) digital output bus operating at 40 MHz.

A digital token is passed sequentially from board to board through a dedicated hardware port to define which circuit board has control of the output bus. This protocol allows all boards in the system to share the same digital output.

E. Bolometer Tuning

The bolometers are tuned by adjusting the bias voltage for each detector and measuring changes in current through the bolometer using the oscillator/demodulator boards. The tuning algorithms are implemented in software running on the readout control computer.

The bolometer tuning takes place after the SQUIDs have been tuned (see §IV B 5) and the LCR_{bolo} resonances have been determined with a network analysis (see §III E).

The first step is to cool the bolometer stage to about ~ 800 mK, which is above the TES transition temperature but below that of the aluminum leads connecting the detectors to the cold multiplexer.

Once this temperature is reached, the detectors are provided with a sufficiently large electrical bias that the devices will remain above their transition temperature when the bolometer stage is cooled to its operating temperature of 250 mK. Since the SQUID dynamic range is not sufficient to handle seven bias carriers simultaneously, the seven detectors in a multiplexer module are biased sequentially. After each bias is turned on, a nulling sinusoid is adjusted to cancel the carrier signal at the SQUID input, before the next TES bias is activated.

The optimum nulling sinusoid amplitude and phase are determined using measurements of both the I and Q components of the demodulated bolometer current as provided by each bolometer’s demodulator and the one-per-multiplexer module “helper” demodulator. After the optimum phase is determined, the “helper” demodulator is no longer needed, and can later be used to tune another channel. Once all seven channels in the multiplexer module are biased and nulled, the bolometer stage temperature is lowered to its operating temperature of ~ 250 mK. The nulling amplitudes are fine-tuned at this temperature to correct for slight impedance changes in the circuit.

The seven bolometers in each module are lowered into their transition sequentially by decreasing the electrical bias power. For a given bolometer, the bias voltage amplitude is decreased while iteratively adjusting the nuller amplitude and phase to keep the current through the SQUID zero (this corrects for the voltage drop across the SQUID input, p5 in Figure 4, as discussed in § III F). This traces out the bolometer current vs. voltage curve (Figure 13). In the upper-right portion of the curve, the TES electrical bias power is sufficient to hold the device above its superconducting transition. As the bias voltage is lowered, the device falls into its transition and is held there by ETF. “Turn-around” is defined as the

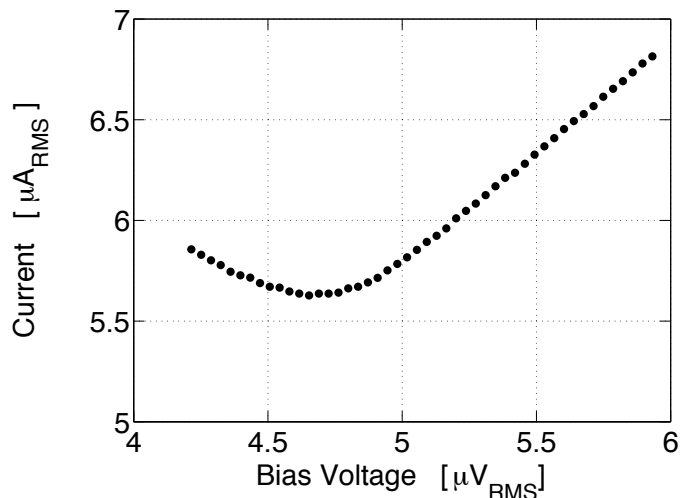


FIG. 13: A current vs. voltage curve is shown for an SPT TES bolometer operating dark at a bath temperature of 0.29 K. In the upper-right portion of the curve, the TES electrical bias power is sufficient to hold the device above its superconducting transition, with constant resistance $\Delta V/\Delta I$. As the bias voltage is lowered, the device falls into its transition and is held there by electro-thermal feedback (ETF). “Turn-around” is defined as the minimum in the curve, about $4.7 \mu\text{V}$, when the dynamic resistance $\partial V/\partial I$ transitions from positive to negative.

minimum in the curve ($4.7 \mu\text{V}$ in Figure 13) when the dynamic impedance $\partial V/\partial I$ transitions from positive to negative (the average TES resistance $\Delta V/\Delta I$ is always positive). At this point the detector ETF loop-gain \mathcal{L} is unity. Once the TES reaches its target operating resistance, the bias voltage is held constant and the current is once again nulled at the SQUID input. All seven bolometers in the multiplexer comb are tuned sequentially in this manner. The tuning of bolometers in different multiplexer modules across the system is performed in parallel. For astronomical observations with SPT (APEX-SZ), the TES sensors are typically operated at 60-80% (80-90%) of their normal resistance corresponding to typical ETF loop-gains $\mathcal{L} \sim 15-20$.

After the electrical bias power of each detector in the system has been decreased so the detectors are operating in their superconducting transition, the demodulator gain is increased from its high dynamic range setting to one of its low noise settings, that has 33-100 times larger gain. The nulling amplitudes are fine-tuned and astronomical observations can commence.

When detector loading conditions change, for example, when a large change in observing elevation is made, adjustments in the nulling may be necessary. Significant changes in detector loading may necessitate re-tuning of the detectors.

V. SYSTEM PERFORMANCE

In this section, measurements of the system performance—including noise, sensitivity, and cross-talk—are presented.

A. System Setup

For SPT and APEX-SZ, the bolometer tuning (described in more detail in § IV E) is integrated with the cycling of the sub-kelvin sorption fridge to minimize the total system setup time. The sorption fridge is cycled every 24–36 hours, elevating the temperature of the bolometers and SQUIDS to above their superconducting transition. This necessitates a re-tuning of the bias parameters for both. The process used for SPT is outlined below.

The SQUIDS are returned to their operating temperature mid-way through the cryogenic cycle and are tuned (§ IV B 5) in parallel with the second half of the cycle. At this point, the bolometers are above their superconducting transition. The SQUIDS are first heated for 30 seconds to release trapped flux and are subsequently allowed to cool quickly through their transition. Following this cooling, it takes about 25 minutes for the SQUIDS to return to their base operating temperature. Next, voltage-current curves (Figure 10) are measured for each SQUID to determine their optimal flux and current bias. For SPT, tuning all 120 SQUIDS takes ~ 25 minutes, and is performed in parallel with the sorption fridge’s cycle, therefore coming at no cost to the observing efficiency.

Towards the end of the cryogenic cycle, the bolometer stage is left at ~ 800 mK so that the detectors are above their superconducting transition. The control computer commands the readout system to bias the detectors with enough electrical power to hold the TES normal and tune the nulling current to cancel the bias at the SQUID input (§ IV E); this takes about 10 minutes. After this, it takes about 2 hours for the sorption fridge to cool the bolometer stage to its ~ 250 mK base temperature. Once the cooling is complete, it takes about 15 minutes to adjust each detector voltage bias to the desired point in its superconducting transition, and then to re-adjust the nulling current (§ IV E). An I-V curve is recorded for each detector (e.g., Figure 13). The total time elapsed for readout/bolometer system tuning and setup is about 25 minutes, not counting the time (several hours) that would otherwise be spent cycling the cryogenics.

SPT has 724 operational detectors. Others have wiring or other defects that prevent their operation. Typically 650 ± 15 of these detectors show good performance each tuning and are used for astronomical observations. Detailed statistics and characterization of end-to-end receiver performance are presented in a separate publication [52].

B. Electrical Cross-Talk

Channel-to-channel cross-talk can occur through optical signals or electrical signals. Optical cross-talk between adjacent bolometers in SPT and APEX-SZ is typically about 1% and is determined by the optical design of the experiment and the arrangement of detectors within a silicon wafer. The goal is for electrical cross-talk arising in the readout system and discussed in § III C to be small in comparison to this optical cross-talk.

Electrical cross-talk in the multiplexer readout has been measured both in the laboratory and during sky-observations. For the laboratory measurement [25], one detector, mounted in its own light-tight enclosure, was excited with light from an LED. Five other sensors were read out on the same fMUX module, but mounted in a separate light-tight enclosure. The absence of any measurable signal in the five dark channels established an upper limit of 0.4% electrical cross-talk.

Cross-talk has been characterized with on-sky observations of RCW38, MAT5A, Venus and Jupiter with the South Pole Telescope. Though we cannot distinguish between positive cross-talk that arises from optical versus electrical sources, negative cross-talk should be dominated by electrical signals. The signal-to-noise levels for RCW38 and MAT5A are substantially lower than for the planets, and no negative cross-talk is observed. Using the observations of Venus and Jupiter, which produce signals that are large enough for small cross-talk signals to be observed in neighbors, a median cross-talk between neighbors of 0.3% is observed. This is consistent with the expectation of 0.25% and 0.3% from mechanisms (2) and (3) described in § III C.

C. Noise Performance

In this section, the measured noise levels for a dark detector in the laboratory and an SPT detector observing the sky are compared with the theoretical expectations.

The noise contributions are divided into three categories: photon noise, bolometer noise, and readout system noise. Within each category, a contribution may arise as a current or power source. Sky signals arise as power sources (photons converted to heat), so that noise equivalent power (NEP) is the relevant metric. Other sources, such as the SQUID noise, are constant in terms of an input referred current, and are labeled here as current noise sources. The NEP of current noise contributors depends on the device parameters and operating conditions and is converted from current to NEP by multiplying the SQUID-input referred current noise by the inverse of the detector responsivity, $\sim -V_{\text{bias}}^{\text{RMS}}/\sqrt{2}$ (see Equation A6 in Appendix A) which is valid in the limit of high loop-gain.

Achieving optimal noise performance with TES bolometers for astronomical observations requires a careful optimization of detector and readout system param-

eters. Most important amongst these is the power required to saturate the detectors, P_{sat} . If this power is many times higher than the absorbed radiation power (or the detector is dark, so that there is no radiation power), thermal phonon noise will be high and relatively large voltage biases must be used to provide the Joule heating necessary to keep the detector in its transition. The high voltage bias results in an amplification of current noise sources when they are referred to NEP, so that the readout component of the noise is greatly enhanced. On the other hand, if P_{sat} is too small, the detector will not have enough dynamic range to operate through a broad range of observing conditions. Typically P_{sat} is set to be roughly twice the expected absorbed incident radiation ($\approx 2 \times P_{\text{rad}}$).

Before describing the noise contributions below, we note that a mixer responds differently to noise that is encoded as a modulation on the carrier and noise that is superimposed on the carrier at the same frequency (see Appendix A). This implementation of the fMUX system uses a square-wave mixer (§ IV C), which introduces a further distinction between (a) broadband noise sources that are superimposed on both the carrier frequency and its harmonics, and (b) narrow-band noise sources that are superimposed on the carrier but do not extend out to the carrier harmonics. SQUID noise is an example of (a) because its bandwidth is not limited. Bolometer Johnson noise is an example of (b) because its bandwidth is limited by the LCR_{bolo} filter. For a square mixer, these noise sources are enhanced in the demodulation process by factors of $\frac{\pi}{2}$ and $\sqrt{2}$ respectively, in comparison to noise that modulates the carrier. Fortunately, in an alternating-voltage biased system, power terms receive an enhancement by a factor $\sqrt{2}$ (with respect to a constant-voltage biased system) during the modulation process, so that the signal-to-noise ratio is nearly unaffected by these factors in comparison to a constant-voltage biased system. Appendix A presents a detailed discussion and derivation of the relevant factors.

1. Dark Noise

In Figure 14 (top, solid line) the noise equivalent power (NEP) density is shown for a representative SPT detector operated in the laboratory with no incident radiation power (“dark”). The detector has a saturation power of $\bar{G}\Delta T \simeq 25$ pW. Its normal resistance $R_{\text{Normal}} = 0.98 \Omega$ and it has been lowered into the transition to $0.73 R_{\text{Normal}}$ with a voltage bias of $4.2 \mu\text{V}_{\text{RMS}}$ (the current-voltage curve for this detector was shown in Figure 13). The roll-off in the measured noise at 35 Hz is due to the readout system’s software low-pass filter described in § IV C.

Noise expectations for this detector are summarized in Table II. Columns are included for dark operation (zero radiation power, shown in the top panel of Figure 14 as a dashed line) and for a radiation loading of 11 pW (shown in the bottom panel of Figure 14 and discussed

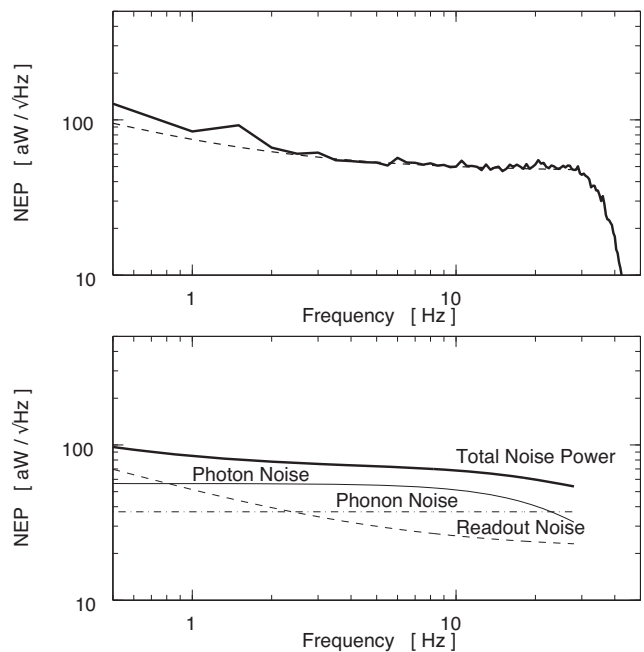


FIG. 14: The measured noise equivalent power (NEP) spectrum density for an SPT TES bolometer operated at $0.73R_{\text{Normal}}$ in the laboratory with no incident radiation (“dark”) is shown (top, solid line) with the theoretical expectation from Table II superimposed (top, dashed line). This configuration represents the worst possible configuration for the readout noise contribution, since the incident power is zero. This means the voltage bias, which refers current noise sources to noise equivalent power, is maximal. In the lower panel the on-sky noise for this detector is estimated assuming a total radiation loading of 11 pW and the detector parameters of Table II. With radiation power, the detector voltage bias is lower and the readout noise is reduced when referred to NEP.

in § V C 2), which is typical of the 150 GHz detectors for SPT. Table II also includes the equations and parameters used to estimate each noise component. A similar table appears in Ref. [2] for APEX-SZ detectors. The noise contributions for “dark” operation are described below.

TES detectors exhibit thermal carrier (or phonon) noise, which arises from random variations in the flow of phonons from the TES to the thermal bath. A factor γ_{NE} has been included in the Table II equation describing this noise to account for a temperature gradient along the thermal link [64]. We have taken $\gamma_{\text{NE}} = 0.5$ [56], consistent with a normal metal link at our operating temperatures. For the dark detector power spectrum density shown in Figure 14, thermal carrier noise dominates above 1 Hz and is eventually cut-off by the TES time constant $\tau_{\text{TES}}^{\text{eff}} \sim 1$ ms, which is not visible in the plot as it is beyond the low-pass filter cut-off.

Both the detector and bias resistor produce Johnson noise in the narrow LCR_{bolo} pass-band that surrounds the carrier. The TES detector Johnson noise current $\sqrt{4k_{\text{B}}T_{\text{bolo}}/R_{\text{bolo}}}$ is superimposed on the amplitude mod-

<i>Detector Parameter:</i>			
TES Transition Temperature	$T_{\text{bolo}}=550 \text{ mK}$		
Thermal Conductivity	$\bar{G} = \frac{\Delta P}{\Delta T} \simeq 96 \text{ pW/K}$	$g_T = \frac{\partial P}{\partial T} \simeq 165 \text{ pW/K}$	
Center Frequency & Bandwidth	$\nu = 153 \text{ GHz}$	$\Delta\nu = 38 \text{ GHz}$	
<i>Detector Setup:</i>		<u>Dark</u>	<u>On-Sky</u>
Bath Temperature		$T_{\text{bath}}=290 \text{ mK}$	$T_{\text{bath}}=260 \text{ mK}$
Incident Radiation Power		$P_{\text{rad}} = 0 \text{ pW}$	$P_{\text{rad}} = 11 \text{ pW}$
TES Normal and operating Resistance	$R_{\text{Normal}} = 0.98 \Omega$	$R_{\text{bolo}} = 0.73 \Omega$	$R_{\text{bolo}} = 0.73 \Omega$
Bias Voltage		$V_{\text{bias}}=4.2 \mu\text{V}_{\text{RMS}}$	$V_{\text{bias}}=3.2 \mu\text{V}_{\text{RMS}}$
Loop-Gain		$\mathcal{L} \simeq 25$	$\mathcal{L} \simeq 15$
Noise Source	Equation	NEP (aW/ $\sqrt{\text{Hz}}$)	
		<u>Dark</u>	<u>On-Sky</u>
<i>Photons:</i>			
Shot noise	$\sqrt{2h\nu P_{\text{rad}}}$	0	47
Correlation noise	$\sqrt{\xi \frac{P_{\text{rad}}^2}{\Delta\nu}}$	0	$\sqrt{\xi} \cdot 56$
<i>Bolometers:</i>			
Thermal Carrier noise ($\gamma_{\text{NE}} = 0.5$)	$\sqrt{\gamma_{\text{NE}} 4k_{\text{B}} T_{\text{bolo}}^2 g_T}$	37	37
Johnson noise	$\sqrt{4k_{\text{B}} T_{\text{bolo}} P_{\text{elec}}/\mathcal{L}}$	$28/\mathcal{L}$	$21/\mathcal{L}$
<i>Readout:</i>			
Warm electronics	$\frac{\pi}{2} \cdot 3.7 \frac{\text{pA}}{\sqrt{\text{Hz}}} \frac{V_{\text{bias}}}{\sqrt{2}}$	17	13
SQUID	$\frac{\pi}{2} \cdot 3.5 \frac{\text{pA}}{\sqrt{\text{Hz}}} \frac{V_{\text{bias}}}{\sqrt{2}}$	16	12
Bias resistor Johnson noise	$\sqrt{2} \cdot 3.1 \frac{\text{pA}}{\sqrt{\text{Hz}}} \frac{V_{\text{bias}}}{\sqrt{2}}$	15	11
<i>Total</i>		47	64,71,85
			($\xi = 0, \xi = 0.3, \xi = 1$)

TABLE II: Theoretical noise equivalent power expectation for a typical SPT detector. The “dark” column corresponds to the operating conditions for the noise spectra recorded in the laboratory and shown in Figure 14, wherein there is no incident radiation. The “on-sky” column corresponds to typical incident radiation power for a 150 GHz SPT detector. Totals are included for several cases of photon correlations ($\xi=0, 0.3$, and 1). A similar table appears in Ref. [2] for APEX-SZ detectors. Device and experiment related parameters are defined at the top of the table, h is Planck’s constant, k_{B} is the Boltzmann constant, ξ is the photon correlation parameter, and γ_{NE} is the non-equilibrium parameter [64].

ulated carrier. For a sinusoidal-biased TES, this Johnson noise beats with the carrier and is mixed down to base-band where its thermal power lies within the detector time constant and is suppressed by electro-thermal feedback. This suppression is similar to that which takes place for a static-biased TES [61], and is derived in Appendix B of Ref. [65]. For the operating parameters of SPT and APEX-SZ detectors, the TES Johnson noise suppression needs to be calculated numerically, but can be approximated by $\sim 1/\mathcal{L}$ for the component that is in-phase with the bias carrier [65] (the out-of-phase component receives no suppression, but is discarded by the demodulator). The bias resistor suppression is less than 20% [65] and has been neglected in the noise expectation tabulated in Table II. For a sinusoidal-biased detector, Johnson noise is enhanced by a factor $\sqrt{2}$ because uncorrelated noise from both sidebands appear

post-demodulation, as discussed in Appendix A. This noise is referred to a noise equivalent power by the inverted responsivity $\sim -V_{\text{bias}}^{\text{RMS}}/\sqrt{2}$. The result is that the total Johnson noise is $\sqrt{4k_{\text{B}} T_{\text{bolo}} P_{\text{elec}}/\mathcal{L}}$, exactly as it would be for a detector biased with a static voltage.

The readout electronics contribute noise from the bias resistor, SQUID, and room temperature electronics as described below. As described in § IV, each multiplexer module bias resistor is located at 4 K adjacent to the SQUIDS (see Figure 1) rather than on the sub-kelvin stage adjacent to the detectors. This higher temperature results in higher Johnson noise from the bias resistor. The advantage is that the number of wires connecting to the sub-kelvin stage is just two per multiplexer comb, rather than the four wires that would be required if the bias resistors were located on the sub-kelvin stage. This noise contribution could be made negligible by using a ca-

capacitive voltage divider [50], an inductive bias, or moving the bias resistor to lower temperature.

The SQUIDs contribute a white noise level of $3.5 \text{ pA}/\sqrt{\text{Hz}}$. Since the detectors are biased at high frequency, the bolometer signals are modulated at frequencies well above the $1/f$ noise of the SQUIDs and pre-mixer amplifiers in the room temperature system. The room temperature electronics noise is $3.7 \text{ pA}/\sqrt{\text{Hz}}$, after being referred back to the bolometer current by the SQUID transimpedance, $Z_{\text{trans}}^{\text{SQ}}$. A higher $Z_{\text{trans}}^{\text{SQ}}$ would reduce this noise that is dominated by the $1 \text{ nV}/\sqrt{\text{Hz}}$ input noise of the first stage amplifier that follows the SQUID inside the flux locked loop. The room temperature electronics noise also receives contributions from Johnson noise in the resistors that set the gain of the amplifiers and convert voltages to currents.

When we account for these noise contributions, the total noise expectation is in good agreement with measurements of dark detectors as shown in Figure 14.

2. On-Sky Noise

The noise expectation for the detector shown in Figure 14, extrapolated to typical SPT 150 GHz observing conditions with 11 pW of incident radiation power, is shown in the “on-sky” column of Table II. This radiation power results in a reduction of the Joule heating necessary to keep the detector at $0.73 R_{\text{Normal}}$, so that the detector is tuned with a lower bias voltage. This lower bias voltage results in a reduced NEP for all current noise sources, such as the three components of readout noise listed in Table II. Since the low frequency noise from the readout system is proportional to the bias voltage amplitude, its amplitude is also reduced. If readout were the only contribution to low-frequency noise, the knee would be at 0.4 Hz for this detector parameters.

In addition to the thermal carrier noise, ETF suppressed Johnson noise, and readout noise, fluctuations in the rate of incident photons produces an additional noise term corresponding to photon shot noise and photon correlations [66, 67], also included in Table II for the “on-sky” detector. The degree of photon correlation depends on poorly characterized details of the filters and coupling, so that the coefficient ξ [68] is often introduced to parametrize a correction factor for the simple equation presented in Table II. ξ lies between 0-1, with 0.3 being a reasonable choice. Table II includes noise expectations spanning the full range.

The power spectrum distribution for a representative 150 GHz bolometer operating “on-sky” during the 2009 observing season on the South Pole Telescope is shown in Figure 15. This data corresponds to the raw timestream; no filtering has been applied to remove atmospheric signals or other effects. The SPT bolometer stage was operated at a bath temperature of $T_{\text{bath}} = 260 \text{ mK}$ and the detector has sufficiently similar device parameters to the dark detector, shown in Figure 14, that its total noise ex-

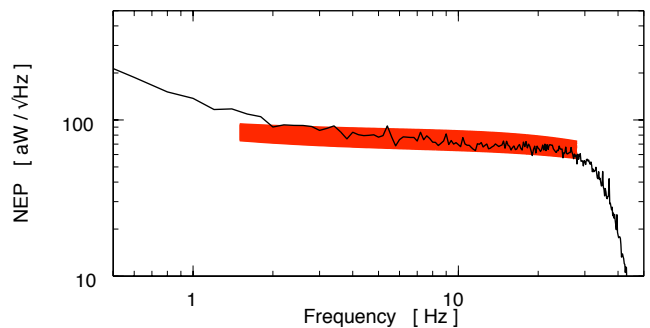


FIG. 15: Power spectrum distribution of a bolometer observing in the 150 GHz band on the South Pole Telescope is shown. The low frequency noise is primarily due to atmospheric fluctuations. This detector’s performance is typical for detectors in the 150 GHz band and agrees well with the expectation, shown as a shaded band. Its measured noise equivalent temperature (NET_{CMB}) is $409 \mu\text{K} \cdot \sqrt{\text{s}}$ projected on the sky.

pectation is the same to within 2% of the values presented in Table 14. Superimposed on Figure 15 is a shaded band corresponding to the noise expectation for this detector, excluding atmospheric contributions. The width of the shaded band indicates the range of allowed photon correlations $0 < \xi < 1$.

At frequencies below $\sim 3 \text{ Hz}$, the spectrum is dominated by atmospheric fluctuations that are not included in the theoretical expectation presented in Table II. For science analyses, filtering and subtraction techniques (see e.g., [33]) applied in the data processing pipeline are used to reduce the effect of atmospheric signals to below 1 Hz . Above this frequency, the spectrum agrees well with the expectation. After calibrating this detector response with astrophysical sources, its measured sensitivity is $409 \mu\text{K}_{\text{CMB}} \cdot \sqrt{\text{s}}$ projected on the sky and referred to a source at the CMB temperature. This is typical of SPT 150 GHz detector performance. Noise and sensitivity statistics for the APEX-SZ and SPT receiver systems are presented in Refs. [52] and [2] respectively.

VI. CONCLUSIONS

We have presented the design and performance of the SQUID-based frequency-domain multiplexed (fMUX) readout system that has been deployed for TES detectors on the APEX-SZ instrument and the South Pole Telescope SZ-camera. The readout reduces the heat-load on the sub-kelvin cryogenic stage by sharing wiring among many detectors using a simple architecture that minimizes the sub-kelvin system complexity. It has near-zero power dissipation on the sub-kelvin stage, is extensible to much higher multiplexing factors, allows bias levels to be set individually for each detector, is modular with no shared components between readout modules, and exhibits strong reduction of microphonic response and low-

frequency EMI because the sky signals are modulated up to high frequency.

The system has been characterized in terms of noise performance, sensitivity, detector yield, and cross-talk in both the laboratory and with on-sky observations. The measured noise equivalent power of the system is consistent with theoretical expectations, and contributions from the readout system are small in comparison to detector and photon noise above 1 Hz. At low frequencies, the system noise is dominated by residual atmospheric fluctuations.

These implementations have shown that frequency-domain multiplexing is an effective technology for scaling to very large arrays of TES detectors. An upgraded digital version of the analog fMUX back-end electronics has recently been developed [51] and has been deployed for the EBEX [69] balloon-borne CMB polarimeter and the ground-based POLARBEAR [70] CMB polarimeter. A polarimeter camera [71] for the South Pole Telescope is being commissioned during the austral 2011/2012 summer and uses the digital fMUX. The digital fMUX system achieves an order of magnitude lower power consumption, higher multiplexing factors, faster detector and SQUID setup, better low frequency noise performance, and lower cost. Development is underway to develop fMUX electronics for satellite applications [72]. Present prototypes use Digital Active Nulling [73] in place of the flux-locked loop. This extends the SQUID bandwidth to allow for 64 bolometers per SQUID module using a single pair of sub-Kelvin wires.

Acknowledgments

We thank Andy Smith for useful discussions and design/fabrication of niobium inductors at Northrup Grumman, Kent Irwin and Gene Hilton for useful discussions and design/fabrication of the series array SQUIDS at NIST, and Hannes Hubmayr, Bryan Steinbach, Kam Arnold, and Graeme Smecher for useful discussions of bolometer responsivity and demodulator response.

The National Science Foundation funds APEX-SZ through grants AST-0138348 & AST-0709497 and the South Pole Telescope through grants ANT-0638937 and ANT-0130612. Work at LBNL is supported by the U.S. Department of Energy under Contract No. DE-AC02-05CH11231. The McGill team acknowledges funding from the Natural Sciences and Engineering Research Council of Canada, Canadian Institute for Advanced Research, and the Canadian Foundation for Innovation. MD acknowledges support from the Canada Research Chairs program and a Sloan Fellowship.

Appendix A: Modulation and demodulation transfer functions for alternating-voltage biased bolometers

In this section, we consider the transfer functions for the modulation and demodulation of signals for a bolometer voltage biased with a constant amplitude sinusoidal carrier. We also consider the transfer function for noise that is superimposed on the amplitude-modulated carrier.

First consider a single Fourier component of a small power signal $P_s \cos \omega_s t$ absorbed by a bolometer that is biased deep in its transition with a constant amplitude voltage bias $V_{\text{bias}} = V_c \sin \omega_c t$.

Under the assumption of strong electro-thermal feedback (ETF), the total power on the detector will be constant and determined by the average thermal conductivity \bar{G} and temperature difference from the bolometer to its bath $\Delta T = T_{\text{bolo}} - T_{\text{bath}}$,

$$P_{\text{TOTAL}} = \bar{G}\Delta T = V_{\text{bias}}I_{\text{bolo}} + P_{\text{rad}} + P_s \cos \omega_s t, \quad (\text{A1})$$

where P_{rad} is the approximately constant radiation loading power from the sky. The amplitude of the bolometer voltage bias is constant, so that the power signal produces an amplitude modulation I_s on the bolometer carrier current I_c :

$$I_{\text{bolo}} = (I_c + I_s \cos \omega_s t) \sin \omega_c t. \quad (\text{A2})$$

Keeping only the time varying terms from Equation A1, the power balance is

$$-P_s \cos \omega_s t = V_c I_s \cos \omega_s t \sin^2(\omega_c t). \quad (\text{A3})$$

Since the carrier frequency ω_c is much faster than the bolometer time constant, the $\sin^2(\omega_c t)$ factor integrates to 1/2, leading to

$$-P_s = \frac{V_c}{2} I_s = \frac{V_c^{\text{RMS}}}{\sqrt{2}} I_s. \quad (\text{A4})$$

Thus, the strong ETF responsivity for a bolometer biased with a sinusoidal voltage is

$$\frac{dI_s}{dP_s} = -\frac{\sqrt{2}}{V_c^{\text{RMS}}} \quad (\text{A5})$$

for amplitude modulated signals. For simplicity, we have left out the factor that accounts for the bolometer time constant. Equation A5 should be compared to $\frac{dI_s}{dP_s} = -\frac{1}{V_c}$ for a constant-voltage biased bolometer [74]. For finite loop-gain \mathcal{L} , the responsivity in Equation A5 becomes

$$\frac{dI_s}{dP_s} = -\frac{\sqrt{2}}{V_c^{\text{RMS}}} \frac{\mathcal{L}}{1 + \mathcal{L}}. \quad (\text{A6})$$

Next we consider a bias carrier waveform $I_c \sin \omega_c t$ and present the response functions for sine-wave demodulation (the traditional mixer reference waveform) and

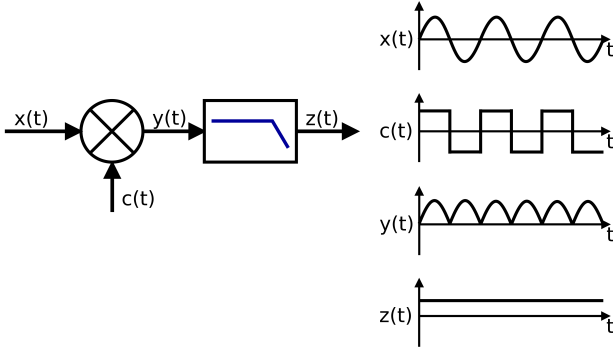


FIG. 16: A generic demodulator, consisting of a mixer and low-pass filter is shown (left). Waveforms for the special case of a sinusoidal input demodulated with a square wave reference is shown at right.

square-wave demodulation (the mixer reference used for this implementation of the fMUX system) as a function of the phase difference between the carrier and the demodulator, ϕ_{ref} . The results for in-phase I demodulation and 90-degree out-of-phase Q demodulation are summarized in Table III.

A generic demodulator is shown in Figure 16 (left), where an input signal $x(t)$ is multiplied by a reference signal $c(t)$ then integrated with a low-pass filter (LPF) to produce the output $z(t)$. The cutoff frequency of the LPF is much lower than the reference frequency and much larger than the modulation-encoded sky-signals.

For the special case of an on-resonance, in-phase sinusoidal input $x(t) = I_c \sin(\omega_c t)$ and a unit amplitude sine-wave reference $c(t) = \sin(\omega_c t)$, the mixer output is the familiar $y(t) = x(t) \times c(t) = I_c \sin^2(\omega_c t) = I_c \frac{1 - \cos 2\omega_c t}{2}$. The LPF averages the second term to zero, so that the demodulator baseband output is $z(t) = I_c/2$.

The $x(t)$, $c(t)$, $y(t)$, and $z(t)$ waveforms are shown for this special case of a square-wave mixer in Figure 16 (right). The reference is an on-resonance, in-phase, unit amplitude square wave $c(t)$. The output is a baseband signal with amplitude equal to the average of a rectified sine wave, $\frac{2}{\pi} I_c$. If the phase of the reference differs from the sinusoid phase by ϕ_{ref} , the amplitude of the baseband output signal $z(t) = \frac{2}{\pi} I_c \cos \phi_{\text{ref}}$, meaning that the response function is $\frac{2}{\pi}$ for in-phase I demodulation and zero for Q .

Figure 17 shows other demodulator input signals that are relevant for understanding the signal and noise transfer functions of the fMUX system. The first case (a) corresponds to a bias carrier $I_c \sin \omega_c t$, $\omega_c \gg \omega_{\text{LPF}}$ modulated by a small sky signal $I_s \cos \omega_s t$, $\omega_s \ll \omega_{\text{LPF}}$, yielding a demodulator input signal

$$\begin{aligned} x(t) &= (I_c + I_s \cos \omega_s t) \sin \omega_c t \\ &= I_c \sin \omega_c t + \frac{I_s}{2} [\sin(\omega_c + \omega_s) + \sin(\omega_c - \omega_s)]. \end{aligned} \quad (\text{A7})$$

This corresponds to the amplitude modulation produced by a power signal discussed in the first part of this Ap-

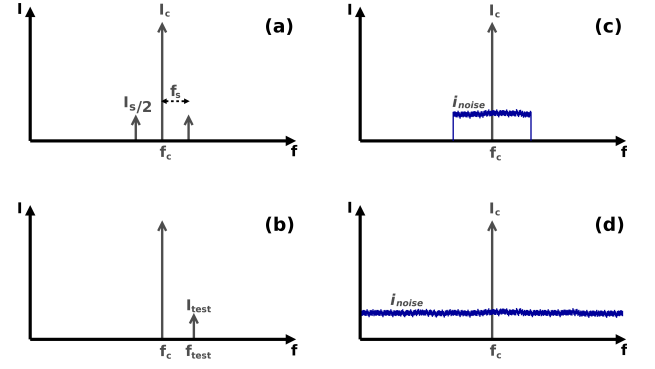


FIG. 17: Frequency-domain representations of (a) a modulation of carrier amplitude I_c with a signal of amplitude I_s , (b) an uncorrelated sinusoid with amplitude I_{test} adjacent to carrier amplitude I_c , (c) narrow-band white noise with amplitude i_{noise} superimposed at frequencies surrounding carrier amplitude I_c , and (d) broadband white noise with amplitude i_{noise} superimposed on carrier amplitude I_c . A fifth case, where narrow-band white noise modulates the carrier (as would be the case for bolometer phonon or photon noise) is not shown.

pendix; and arises from sky signals, bolometer phonon noise, and bolometer photon noise. The sky signal is split into correlated sidebands adjacent to the carrier and appears in the demodulated timestream with amplitude $z(t) = \frac{2}{\pi} I_s \cos \phi_{\text{ref}} \cos \omega_s t$.

Case (b) in Figure 17 corresponds to an off-resonance sinusoid $I_t \sin \omega_t t$ injected adjacent to the carrier. For simplicity, this test sinusoid is assumed to be injected after the bolometer so that the sinusoid does not deposit power in the bolometer that would be subject to ETF. The test sinusoid beats with the carrier so that the demodulated signal is $z(t) = \frac{1}{2} I_t \cos \phi_{\text{ref}} \sin |\omega_t - \omega_c| t$ for a sine-wave mixer and $z(t) = \frac{2}{\pi} I_t \cos \phi_{\text{ref}} \sin |\omega_t - \omega_c| t$ for a square-wave mixer. Notice that the test signal has the same demodulation attenuation factor as an on-resonance amplitude modulated signal. Test signals of this type are used extensively in the fMUX system for measuring electronics transfer functions and characterizing detectors.

The situation for white noise added to the carrier waveform (i.e., does not amplitude-modulate the carrier) requires special attention, because it differs from noise that amplitude modulates the carrier and because the square-wave mixer responds differently to broadband and narrow-band noise sources.

Case (c) in Figure 17 corresponds to bandwidth limited white noise adjacent to the carrier with amplitude $x(t) = i_{\text{noise}} [A/\sqrt{\text{Hz}}]$. An example would be Johnson noise from a resistor in an LCR notch filter (or from a normal bolometer in our fMUX circuit, though ETF complicates the situation for a bolometer in transition, suppressing this noise). A single sideband can be decomposed into sinusoids, and hence has the same response function as case (b). There are, however, contributions from the sidebands on either side of the carrier, each

Input Signal $x(t)$		$c(t)$ = Square-wave reference		$c(t) = \sin(\omega_c t)$ reference	
		I	Q	I	Q
Sinusoidal carrier	$I_c \sin \omega_c t$	$\frac{2}{\pi} I_c$	0	$\frac{1}{2} I_c$	0
Amplitude modulated carrier (a)	$(I_c + I_s \cos \omega_s t) \sin \omega_c t$	$\frac{2(I_c + I_s \cos \omega_s t)}{\pi}$	0	$\frac{I_c + I_s \cos \omega_s t}{2}$	0
Sinusoidal test signal (b)	$I_t \sin \omega_t t, \omega_t \neq \omega_d$	$\dagger \frac{2}{\pi} I_t \sin(\omega_t - \omega_c) t$		$\dagger \frac{1}{2} I_t \sin(\omega_t - \omega_c) t$	
Superimposed narrowband white noise (c)	$n(t)$	$\frac{2\sqrt{2}}{\pi} n(t)$		$\frac{\sqrt{2}}{2} n(t)$	
Superimposed broadband white noise (d)	$n(t)$	$n(t)$		$\frac{\sqrt{2}}{2} n(t)$	

TABLE III: Demodulator response factors are tabulated for various signal and noise types including those shown in panels (a) through (d) of Figure 17. ω_c is the demodulator reference frequency. Notice that white noise that is superimposed on the carrier (not amplitude modulated) has a factor $\sqrt{2}$ enhancement over amplitude modulated signals. For the case of a square mixer and broadband white noise, the factor is $\frac{\pi}{2}$ because noise located within the LPF bandwidth of the reference signal's odd harmonics also contribute.

† An arbitrary phase which depends on the start time is omitted from these equations.

contributing the same power. The two sidebands are uncorrelated with one another, resulting in a $\sqrt{2}$ enhancement, for a total contribution $z(t) = \frac{\sqrt{2}}{2} i_{\text{noise}}$ for a sine-wave mixer and $z(t) = \frac{2\sqrt{2}}{\pi} i_{\text{noise}}$ for a square-wave mixer. There is no dependence on ϕ_{ref} since this input signal is not coherent. The end result is that the sky-signal to narrow-band noise ratio is the same for a TES read out through a square-wave mixer and a sine-wave mixer, and equivalent to what would be obtained for a TES with a static bias.

Case (d) in Figure 17 corresponds to broadband white noise with amplitude $i_{\text{noise}}[\text{A}/\sqrt{\text{Hz}}]$. An example would be SQUID noise or readout electronics noise. For a sine-wave mixer, the response is identical to that of case (c). For a square-wave mixer, both the noise power adjacent to the carrier *and* the noise power adjacent to the odd-harmonics of the carrier contribute. This is immediately evident by examining the frequency-space representation of the square-wave, which includes delta functions at all of the odd-harmonics that fall in amplitude as $1/n$. Since

the noise waveform is characterized by random phase and the square-wave mixer simply rotates the phase of half the time samples by 180° , it is easy to see that the demodulated amplitude will be unchanged, $z(t) = i_{\text{noise}}$. We note that the demodulated amplitude of broadband noise can be reduced to that of case (c) if the carriers span less than 2 octaves by placing a low-pass filter in front of the mixer, removing input from the 3^{rd} harmonics. The end result is that the sky-signal to narrow-band noise ratio is the same for a TES readout out through a square-wave mixer and a sine-wave mixer, and equivalent to what would be obtained for a TES with a static bias. The end result is that the sky-signal to broadband noise ratio is $(2/\pi)/(1/\sqrt{2}) \simeq 0.90$ worse for a TES read out through a square-wave mixer as compared to a sine-wave mixer. The latter is equivalent to what would be obtained for a TES with a static bias. Typically for fMUX readout, the contribution from broadband noise sources is small, and this difference is negligible.

- [1] D. S. Swetz, P. A. R. Ade, M. Amiri, J. W. Appel, E. S. Battistelli, B. Burger, J. Chervenak, M. J. Devlin, S. R. Dicker, W. B. Doriese, R. Dünner, T. Essinger-Hileman, R. P. Fisher, J. W. Fowler, M. Halpern, M. Hasselfield, G. C. Hilton, A. D. Hincks, K. D. Irwin, N. Jarosik, M. Kaul, J. Klein, J. M. Lau, M. Limon, T. A. Marriage, D. Marsden, K. Martocci, P. Mauskopf, H. Moseley, C. B. Netterfield, M. D. Niemack, M. R. Nolta, L. A. Page, L. Parker, S. T. Staggs, O. Stryzak, E. R. Switzer, R. Thornton, C. Tucker, E. Wollack, and Y. Zhao, *Astrophys. J.* **194**, 41 (2011).
- [2] D. Schwan *et al.* (The APEX-SZ Collaboration), *Rev. Sci. Instrum.* **82**, 091301 (2011).

- [3] Y. D. Takahashi, P. A. R. Ade, D. Barkats, J. O. Battle, E. M. Bierman, J. J. Bock, H. C. Chiang, C. D. Dowell, L. Duband, E. F. Hivon, W. L. Holzapfel, V. V. Hristov, W. C. Jones, B. G. Keating, J. M. Kovac, C. L. Kuo, A. E. Lange, E. M. Leitch, P. V. Mason, T. Matsumura, H. T. Nguyen, N. Ponthieu, C. Pryke, S. Richter, G. Rocha, and K. W. Yoon, *Astrophys. J.* **711**, 1141 (2010).
- [4] J. E. Carlstrom, P. A. R. Ade, K. A. Aird, B. A. Benson, L. E. Bleem, S. Busetti, C. L. Chang, E. Chauvin, H.-M. Cho, T. M. Crawford, A. T. Crites, M. A. Dobbs, N. W. Halverson, S. Heimsath, W. L. Holzapfel, J. D. Hrubes, M. Joy, R. Keisler, T. M. Lanting, A. T. Lee,

- E. M. Leitch, J. Leong, W. Lu, M. Lueker, D. Luongvan, J. J. McMahon, J. Mehl, S. S. Meyer, J. J. Mohr, T. E. Montroy, S. Padin, T. Plagge, C. Pryke, J. E. Ruhl, K. K. Schaffer, D. Schwan, E. Shirokoff, H. G. Spieler, Z. Staniszewski, A. A. Stark, C. Tucker, K. Vanderlinde, J. D. Vieira, and R. Williamson, *Publ. Astron. Soc. Pac.* **123**, 568 (2011).
- [5] A. T. Lee, H. Tran, P. Ade, K. Arnold, J. Borrill, M. A. Dobbs, J. Errard, N. Halverson, W. L. Holzapfel, J. Howard, A. Jaffe, B. Keating, Z. Kermish, E. Linder, N. Miller, M. Myers, A. Niarchou, H. Paar, C. Reichardt, H. Spieler, B. Steinbach, R. Stompor, C. Tucker, E. Quealy, P. L. Richards, and O. Zahn, POLARBEAR: Ultra-high Energy Physics with Measurements of CMB Polarization, in *AIP Conf. Proc.*, volume 1040, pages 66–77, 2008.
- [6] W. Holland, M. MacIntosh, A. Fairley, D. Kelly, D. Montgomery, D. Gostick, E. Atad-Ettedgui, M. Ellis, I. Robson, M. Hollister, A. Woodcraft, P. Ade, I. Walker, K. Irwin, G. Hilton, W. Duncan, C. Reintsema, A. Walton, W. Parkes, C. Dunare, M. Fich, J. Kyrcia, M. Halpern, D. Scott, A. Gibb, J. Molnar, E. Chapin, D. Bintley, S. Craig, T. Chylek, T. Jenness, F. Economou, and G. Davis, SCUBA-2: a 10,000-pixel submillimeter camera for the James Clerk Maxwell Telescope, in *Proc. SPIE Int. Soc. Opt. Eng.*, volume 6275, page 62751E, 2006.
- [7] R. Sultan, B. L. Zink, K. D. Irwin, G. C. Hilton, J. N. Ullom, and L. R. Vale, *J. Low Temp. Phys.* **151**, 363 (2008).
- [8] W. B. Doriese, J. N. Ullom, J. A. Beall, W. D. Duncan, L. Ferreira, G. C. Hilton, R. D. Horansky, K. D. Irwin, J. A. B. Mates, C. D. Reintsema, L. R. Vale, Y. Xu, B. L. Zink, M. W. Rabin, A. S. Hoover, C. R. Rudy, and D. T. Vo, *Appl. Phys. Lett.* **90**, 193508 (2007).
- [9] W. B. Doriese, J. A. Beall, S. Deiker, W. D. Duncan, L. Ferreira, G. C. Hilton, K. D. Irwin, C. D. Reintsema, J. N. Ullom, L. R. Vale, and Y. Xu, *Appl. Phys. Lett.* **85**, 4762 (2004).
- [10] J. Dreyer, K. Arnold, T. Lanting, M. Dobbs, S. Friedrich, A. Lee, and H. Spieler, *IEEE Trans. Appl. Supercond.* **17**, 633 (2007).
- [11] N. Wang, *Physica B* **165**, 3 (1990).
- [12] J. A. Chervenak, K. D. Irwin, E. N. Grossman, J. M. Martinis, C. D. Reintsema, and M. E. Huber, *Appl. Phys. Lett.* **74**, 4043 (1999).
- [13] J. A. Chervenak, E. N. Grossman, K. D. Irwin, J. M. Martinis, C. D. Reintsema, C. A. Allen, D. I. Bergman, S. H. Moseley, and R. Shafer, *Nucl. Instrum. Meth. A* **444**, 107 (2000).
- [14] K. D. Irwin, L. R. Vale, N. E. Bergren, S. Deiker, E. N. Grossman, G. C. Hilton, S. W. Nam, C. D. Reintsema, D. A. Rudman, and M. E. Huber, Time-division SQUID multiplexers, in *AIP Conf. Proc.*, volume 605, pages 301–304, 2002.
- [15] E. S. Battistelli, M. Amiri, B. Burger, M. Halpern, S. Knotek, M. Ellis, X. Gao, D. Kelly, M. Macintosh, K. Irwin, and C. Reintsema, *J. Low Temp. Phys.* **151**, 908 (2008).
- [16] J. G. Staguhn, D. J. Benford, F. Pajot, T. J. Ames, J. A. Chervenak, E. N. Grossman, K. D. Irwin, B. Maffei, S. H. Moseley, T. G. Phillips, C. D. Reintsema, C. Rioux, R. A. Shafer, and G. M. Voellmer, Astronomical demonstration of superconducting bolometer arrays, in *Proc. SPIE Int. Soc. Opt. Eng.* **4855**, 100–107 (2003).
- [17] K. D. Irwin and K. W. Lehnert, *Appl. Phys. Lett.* **85**, 2107 (2004).
- [18] K. D. Irwin, J. A. Beall, W. B. Doriese, W. D. Duncan, G. C. Hilton, J. A. B. Mates, C. D. Reintsema, D. R. Schmidt, J. N. Ullom, L. R. Vale, B. L. Zink, and K. W. Lehnert, *Nucl. Instrum. Meth. A* **559**, 802 (2006).
- [19] K. D. Irwin, M. D. Niemack, J. Beyer, H. M. Cho, W. B. Doriese, G. C. Hilton, C. D. Reintsema, D. R. Schmidt, J. N. Ullom, and L. R. Vale, *Supercond. Sci. Technol.* **23**, 034004 (2010).
- [20] J. Yoon, J. Clarke, J. M. Gildemeister, A. T. Lee, M. J. Myers, P. L. Richards, and J. T. Skidmore, *Appl. Phys. Lett.* **78**, 371 (2001).
- [21] J. Yoon, J. Clarke, J. M. Gildemeister, A. T. Lee, M. J. Myers, P. L. Richards, J. T. Skidmore, and H. G. Spieler, Single SQUID multiplexer for arrays of Voltage-biased Superconducting Bolometers, in *AIP Conf. Proc.*, volume 605, pages 305–308, 2002.
- [22] H. Spieler, Frequency domain multiplexing for large scale bolometer arrays, in *Monterey Far-IR, Sub-mm and mm Detector Technology Workshop proceedings*, edited by J. Wolf, J. Farhoomand, and C. McCreight, 243–249 (2002, NASA).
- [23] T. M. Lanting, H. Cho, J. Clarke, M. Dobbs, A. T. Lee, P. L. Richards, H. Spieler, and A. Smith, Frequency-domain multiplexing for large-scale bolometer arrays, in *Proc. SPIE Int. Soc. Opt. Eng.*, volume 4855, pages 172–181, 2003.
- [24] T. M. Lanting, H. Cho, J. Clarke, M. Dobbs, A. T. Lee, M. Lueker, P. L. Richards, A. D. Smith, and H. G. Spieler, *Nucl. Instrum. Meth. A* **520**, 548 (2004).
- [25] T. M. Lanting, H.-M. Cho, J. Clarke, W. L. Holzapfel, A. T. Lee, M. Lueker, P. L. Richards, M. A. Dobbs, H. Spieler, and A. Smith, *Appl. Phys. Lett.* **86**, 112511 (2005).
- [26] T. M. Lanting, K. Arnold, H.-M. Cho, J. Clarke, M. Dobbs, W. Holzapfel, A. T. Lee, M. Lueker, P. L. Richards, A. D. Smith, and H. G. Spieler, *Nucl. Instrum. Meth. A* **559**, 793 (2006).
- [27] T. M. Lanting, *Multiplexed readout of superconducting bolometers for cosmological observations*, PhD thesis, University of California, Berkeley, 2006.
- [28] M. Dobbs, N. W. Halverson, P. A. R. Ade, K. Basu, A. Beelen, F. Bertoldi, C. Cohalan, H. M. Cho, R. Güsten, W. L. Holzapfel, Z. Kermish, R. Kneissl, A. Kovács, E. Kreysa, T. M. Lanting, A. T. Lee, M. Lueker, J. Mehl, K. M. Menten, D. Muders, M. Nord, T. Plagge, P. L. Richards, P. Schilke, D. Schwan, H. Spieler, A. Weiss, and M. White, *New Astron. Rev.* **50**, 960 (2006).
- [29] D. Schwan for the APEX-SZ Collaboration, *New Astron. Rev.* **47**, 933 (2003).
- [30] J.E. Ruhl for the SPT Collaboration, The South Pole Telescope, in *Proc. SPIE Int. Soc. Opt. Eng.*, volume 5494, pages 11–29, 2004.
- [31] R. A. Sunyaev and Y. B. Zeldovich, *Comments Astrophys. Space Phys.* **4**, 173 (1972).
- [32] N. W. Halverson, T. Lanting, P. A. R. Ade, K. Basu, A. N. Bender, B. A. Benson, F. Bertoldi, H. M. Cho, G. Chon, J. Clarke, M. Dobbs, D. Ferrusca, R. Guesten, W. L. Holzapfel, A. Kovacs, J. Kennedy, Z. Kermish, R. Kneissl, A. T. Lee, M. Lueker, J. Mehl, K. M. Menten, D. Muders, M. Nord, F. Pacaud, T. Plagge, C. Re-

- ichardt, P. L. Richards, R. Schaaf, P. Schilke, F. Schuller, D. Schwan, H. Spieler, C. Tucker, A. Weiss, and O. Zahn, *Astrophys. J.* **701**, 42 (2009).
- [33] Z. Staniszewski, P. A. R. Ade, K. A. Aird, B. A. Benson, L. E. Bleem, J. E. Carlstrom, C. L. Chang, H. Cho, T. M. Crawford, A. T. Crites, T. de Haan, M. A. Dobbs, N. W. Halverson, G. P. Holder, W. L. Holzapfel, J. D. Hrubes, M. Joy, R. Keisler, T. M. Lanting, A. T. Lee, E. M. Leitch, A. Loehr, M. Lueker, J. J. McMahon, J. Mehl, S. S. Meyer, J. J. Mohr, T. E. Montroy, C. Ngeow, S. Padin, T. Plagge, C. Pryke, C. L. Reichardt, J. E. Ruhl, K. K. Schaffer, L. Shaw, E. Shirokoff, H. G. Spieler, B. Stalder, A. A. Stark, K. Vanderlinde, J. D. Vieira, O. Zahn, and A. Zenteno, *Astrophys. J.* **701**, 32 (2009).
- [34] C. L. Reichardt, L. Shaw, O. Zahn, K. A. Aird, B. A. Benson, L. E. Bleem, J. E. Carlstrom, C. L. Chang, H. M. Cho, T. M. Crawford, A. T. Crites, T. de Haan, M. A. Dobbs, J. Dudley, E. M. George, N. W. Halverson, G. P. Holder, W. L. Holzapfel, S. Hoover, Z. Hou, J. D. Hrubes, M. Joy, R. Keisler, L. Knox, A. T. Lee, E. M. Leitch, M. Lueker, D. Luong-Van, J. J. McMahon, J. Mehl, S. S. Meyer, M. Millea, J. J. Mohr, T. E. Montroy, T. Natoli, S. Padin, T. Plagge, C. Pryke, J. E. Ruhl, K. K. Schaffer, E. Shirokoff, H. G. Spieler, Z. Staniszewski, A. A. Stark, K. Story, A. van Engelen, K. Vanderlinde, J. D. Vieira, and R. Williamson, to appear in *Astrophys. J.* 2012, [arXiv:1111.0932].
- [35] R. Keisler, C. L. Reichardt, K. A. Aird, B. A. Benson, L. E. Bleem, J. E. Carlstrom, C. L. Chang, H. M. Cho, T. M. Crawford, A. T. Crites, T. de Haan, M. A. Dobbs, J. Dudley, E. M. George, N. W. Halverson, G. P. Holder, W. L. Holzapfel, S. Hoover, Z. Hou, J. D. Hrubes, M. Joy, L. Knox, A. T. Lee, E. M. Leitch, M. Lueker, D. Luong-Van, J. J. McMahon, J. Mehl, S. S. Meyer, M. Millea, J. J. Mohr, T. E. Montroy, T. Natoli, S. Padin, T. Plagge, C. Pryke, J. E. Ruhl, K. K. Schaffer, L. Shaw, E. Shirokoff, H. G. Spieler, Z. Staniszewski, A. A. Stark, K. Story, A. van Engelen, K. Vanderlinde, J. D. Vieira, R. Williamson, and O. Zahn, *Astrophys. J.* **743**, 28 (2011).
- [36] K. Story, K. A. Aird, K. Andersson, R. Armstrong, G. Bazin, B. A. Benson, L. E. Bleem, M. Bonamente, M. Brodwin, J. E. Carlstrom, C. L. Chang, A. Clocchiatti, T. M. Crawford, A. T. Crites, T. de Haan, S. Desai, M. A. Dobbs, J. P. Dudley, R. J. Foley, E. M. George, M. D. Gladders, A. H. Gonzalez, N. W. Halverson, F. W. High, G. P. Holder, W. L. Holzapfel, S. Hoover, J. D. Hrubes, M. Joy, R. Keisler, L. Knox, A. T. Lee, E. M. Leitch, M. Lueker, D. Luong-Van, D. P. Marrone, J. J. McMahon, J. Mehl, S. S. Meyer, J. J. Mohr, T. E. Montroy, S. Padin, T. Plagge, C. Pryke, C. L. Reichardt, A. Rest, J. Ruel, J. E. Ruhl, B. R. Saliwanchik, A. Saro, K. K. Schaffer, L. Shaw, E. Shirokoff, J. Song, H. G. Spieler, B. Stalder, Z. Staniszewski, A. A. Stark, C. W. Stubbs, K. Vanderlinde, J. D. Vieira, R. Williamson, and A. Zenteno, *Astrophys. J. Lett.* **735**, L36 (2011).
- [37] R. Williamson, B. A. Benson, F. W. High, K. Vanderlinde, P. A. R. Ade, K. A. Aird, K. Andersson, R. Armstrong, M. L. N. Ashby, M. Bautz, G. Bazin, E. Bertin, L. E. Bleem, M. Bonamente, M. Brodwin, J. E. Carlstrom, C. L. Chang, S. C. Chapman, A. Clocchiatti, T. M. Crawford, A. T. Crites, T. de Haan, S. Desai, M. A. Dobbs, J. P. Dudley, G. G. Fazio, R. J. Foley, W. R. Forman, G. Garmire, E. M. George, M. D. Gladders, A. H. Gonzalez, N. W. Halverson, G. P. Holder, W. L. Holzapfel, S. Hoover, J. D. Hrubes, C. Jones, M. Joy, R. Keisler, L. Knox, A. T. Lee, E. M. Leitch, M. Lueker, D. P. Marrone, J. J. McMahon, J. Mehl, S. S. Meyer, J. J. Mohr, T. E. Montroy, S. S. Murray, S. Padin, T. Plagge, C. Pryke, C. L. Reichardt, A. Rest, J. Ruel, J. E. Ruhl, K. K. Schaffer, L. Shaw, E. Shirokoff, J. Song, H. G. Spieler, B. Stalder, Z. Staniszewski, A. A. Stark, C. W. Stubbs, K. Vanderlinde, J. D. Vieira, A. Vikhlinin, R. Williamson, Y. Yang, O. Zahn, and A. Zenteno, *Astrophys. J.* **738**, 48 (2011).
- [38] E. Shirokoff, C. L. Reichardt, L. Shaw, M. Millea, P. A. R. Ade, K. A. Aird, B. A. Benson, L. E. Bleem, J. E. Carlstrom, C. L. Chang, H. M. Cho, T. M. Crawford, A. T. Crites, T. de Haan, M. A. Dobbs, J. Dudley, E. M. George, N. W. Halverson, G. P. Holder, W. L. Holzapfel, J. D. Hrubes, M. Joy, R. Keisler, L. Knox, A. T. Lee, E. M. Leitch, M. Lueker, D. Luong-Van, J. J. McMahon, J. Mehl, S. S. Meyer, J. J. Mohr, T. E. Montroy, S. Padin, T. Plagge, C. Pryke, J. E. Ruhl, K. K. Schaffer, H. G. Spieler, Z. Staniszewski, A. A. Stark, K. Story, K. Vanderlinde, J. D. Vieira, R. Williamson, and O. Zahn, *Astrophys. J.* **736**, 61 (2011).
- [39] M. Brodwin, J. Ruel, P. A. R. Ade, K. A. Aird, K. Andersson, M. L. N. Ashby, M. Bautz, G. Bazin, B. A. Benson, L. E. Bleem, J. E. Carlstrom, C. L. Chang, T. M. Crawford, A. T. Crites, T. de Haan, S. Desai, M. A. Dobbs, J. P. Dudley, G. G. Fazio, R. J. Foley, W. R. Forman, G. Garmire, E. M. George, M. D. Gladders, A. H. Gonzalez, N. W. Halverson, F. W. High, G. P. Holder, W. L. Holzapfel, J. D. Hrubes, C. Jones, M. Joy, R. Keisler, L. Knox, A. T. Lee, E. M. Leitch, M. Lueker, D. P. Marrone, J. J. McMahon, J. Mehl, S. S. Meyer, J. J. Mohr, T. E. Montroy, S. S. Murray, S. Padin, T. Plagge, C. Pryke, C. L. Reichardt, A. Rest, J. E. Ruhl, K. K. Schaffer, L. Shaw, E. Shirokoff, J. Song, H. G. Spieler, B. Stalder, S. A. Stanford, Z. Staniszewski, A. A. Stark, C. W. Stubbs, K. Vanderlinde, J. D. Vieira, A. Vikhlinin, R. Williamson, Y. Yang, O. Zahn, and A. Zenteno, *Astrophys. J.* **721**, 90 (2010).
- [40] K. Andersson, B. A. Benson, P. A. R. Ade, K. A. Aird, B. Armstrong, M. Bautz, L. E. Bleem, M. Brodwin, J. E. Carlstrom, C. L. Chang, T. M. Crawford, A. T. Crites, T. de Haan, S. Desai, M. A. Dobbs, J. P. Dudley, R. J. Foley, W. R. Forman, G. Garmire, E. M. George, M. D. Gladders, N. W. Halverson, F. W. High, G. P. Holder, W. L. Holzapfel, J. D. Hrubes, C. Jones, M. Joy, R. Keisler, L. Knox, A. T. Lee, E. M. Leitch, M. Lueker, D. P. Marrone, J. J. McMahon, J. Mehl, S. S. Meyer, J. J. Mohr, T. E. Montroy, S. S. Murray, S. Padin, T. Plagge, C. Pryke, C. L. Reichardt, A. Rest, J. Ruel, J. E. Ruhl, K. K. Schaffer, L. Shaw, E. Shirokoff, J. Song, H. G. Spieler, B. Stalder, Z. Staniszewski, A. A. Stark, C. W. Stubbs, K. Vanderlinde, J. D. Vieira, A. Vikhlinin, R. Williamson, Y. Yang, O. Zahn, and A. Zenteno, *Astrophys. J.* **738**, 48 (2011).
- [41] K. Vanderlinde, T. M. Crawford, T. de Haan, J. P. Dudley, L. Shaw, P. A. R. Ade, K. A. Aird, B. A. Benson, L. E. Bleem, M. Brodwin, J. E. Carlstrom, C. L. Chang, A. T. Crites, S. Desai, M. A. Dobbs, R. J. Foley, E. M. George, M. D. Gladders, N. R. Hall, N. W. Halverson, F. W. High, G. P. Holder, W. L. Holzapfel, J. D. Hrubes, M. Joy, R. Keisler, L. Knox, A. T. Lee, E. M. Leitch,

- A. Loehr, M. Lueker, D. P. Marrone, J. J. McMahon, J. Mehl, S. S. Meyer, J. J. Mohr, T. E. Montroy, C.-C. Ngeow, S. Padin, T. Plagge, C. Pryke, C. L. Reichardt, A. Rest, J. Ruel, J. E. Ruhl, K. K. Schaffer, E. Shirokoff, J. Song, H. G. Spieler, B. Stalder, Z. Staniszewski, A. A. Stark, C. W. Stubbs, A. van Engelen, J. D. Vieira, R. Williamson, Y. Yang, O. Zahn, and A. Zenteno, *Astrophys. J.* **722**, 1180 (2010).
- [42] F. W. High, B. Stalder, J. Song, P. A. R. Ade, K. A. Aird, S. S. Allam, R. Armstrong, W. A. Barkhouse, B. A. Benson, E. Bertin, S. Bhattacharya, L. E. Bleem, M. Brodwin, E. J. Buckley-Geer, J. E. Carlstrom, P. Challis, C. L. Chang, T. M. Crawford, A. T. Crites, T. de Haan, S. Desai, M. A. Dobbs, J. P. Dudley, R. J. Foley, E. M. George, M. Gladders, N. W. Halverson, M. Hamuy, S. M. Hansen, G. P. Holder, W. L. Holzapfel, J. D. Hrubes, M. Joy, R. Keisler, A. T. Lee, E. M. Leitch, H. Lin, Y.-T. Lin, A. Loehr, M. Lueker, D. Marrone, J. J. McMahon, J. Mehl, S. S. Meyer, J. J. Mohr, T. E. Montroy, N. Morell, C.-C. Ngeow, S. Padin, T. Plagge, C. Pryke, C. L. Reichardt, A. Rest, J. Ruel, J. E. Ruhl, K. K. Schaffer, L. Shaw, E. Shirokoff, R. C. Smith, H. G. Spieler, Z. Staniszewski, A. A. Stark, C. W. Stubbs, D. L. Tucker, K. Vanderlinde, J. D. Vieira, R. Williamson, W. M. Wood-Vasey, Y. Yang, O. Zahn, and A. Zenteno, *Astrophys. J.* **723**, 1736 (2010).
- [43] M. Lueker, C. L. Reichardt, K. K. Schaffer, O. Zahn, P. A. R. Ade, K. A. Aird, B. A. Benson, L. E. Bleem, J. E. Carlstrom, C. L. Chang, H.-M. Cho, T. M. Crawford, A. T. Crites, T. de Haan, M. A. Dobbs, E. M. George, N. R. Hall, N. W. Halverson, G. P. Holder, W. L. Holzapfel, J. D. Hrubes, M. Joy, R. Keisler, L. Knox, A. T. Lee, E. M. Leitch, J. J. McMahon, J. Mehl, S. S. Meyer, J. J. Mohr, T. E. Montroy, S. Padin, T. Plagge, C. Pryke, J. E. Ruhl, L. Shaw, E. Shirokoff, H. G. Spieler, B. Stalder, Z. Staniszewski, A. A. Stark, K. Vanderlinde, J. D. Vieira, and R. Williamson, *Astrophys. J.* **719**, 1045 (2010).
- [44] N. R. Hall, R. Keisler, L. Knox, C. L. Reichardt, P. A. R. Ade, K. A. Aird, B. A. Benson, L. E. Bleem, J. E. Carlstrom, C. L. Chang, H.-M. Cho, T. M. Crawford, A. T. Crites, T. de Haan, M. A. Dobbs, E. M. George, N. W. Halverson, G. P. Holder, W. L. Holzapfel, J. D. Hrubes, M. Joy, A. T. Lee, E. M. Leitch, M. Lueker, J. J. McMahon, J. Mehl, S. S. Meyer, J. J. Mohr, T. E. Montroy, S. Padin, T. Plagge, C. Pryke, J. E. Ruhl, K. K. Schaffer, L. Shaw, E. Shirokoff, H. G. Spieler, B. Stalder, Z. Staniszewski, A. A. Stark, E. R. Switzer, K. Vanderlinde, J. D. Vieira, R. Williamson, and O. Zahn, *Astrophys. J.* **718**, 632 (2010).
- [45] J. D. Vieira, T. M. Crawford, E. R. Switzer, P. A. R. Ade, K. A. Aird, M. L. N. Ashby, B. A. Benson, L. E. Bleem, M. Brodwin, J. E. Carlstrom, C. L. Chang, H.-M. Cho, A. T. Crites, T. de Haan, M. A. Dobbs, W. Everett, E. M. George, M. Gladders, N. R. Hall, N. W. Halverson, F. W. High, G. P. Holder, W. L. Holzapfel, J. D. Hrubes, M. Joy, R. Keisler, L. Knox, A. T. Lee, E. M. Leitch, M. Lueker, D. P. Marrone, V. McIntyre, J. J. McMahon, J. Mehl, S. S. Meyer, J. J. Mohr, T. E. Montroy, S. Padin, T. Plagge, C. Pryke, C. L. Reichardt, J. E. Ruhl, K. K. Schaffer, L. Shaw, E. Shirokoff, H. G. Spieler, B. Stalder, Z. Staniszewski, A. A. Stark, K. Vanderlinde, W. Walsh, R. Williamson, Y. Yang, O. Zahn, and A. Zenteno, *Astrophys. J.* **719**, 763 (2010).
- [46] T. Plagge, B. A. Benson, P. A. R. Ade, K. A. Aird, L. E. Bleem, J. E. Carlstrom, C. L. Chang, H.-M. Cho, T. M. Crawford, A. T. Crites, T. de Haan, M. A. Dobbs, E. M. George, N. R. Hall, N. W. Halverson, G. P. Holder, W. L. Holzapfel, J. D. Hrubes, M. Joy, R. Keisler, L. Knox, A. T. Lee, E. M. Leitch, M. Lueker, D. Marrone, J. J. McMahon, J. Mehl, S. S. Meyer, J. J. Mohr, T. E. Montroy, S. Padin, C. Pryke, C. L. Reichardt, J. E. Ruhl, K. K. Schaffer, L. Shaw, E. Shirokoff, H. G. Spieler, B. Stalder, Z. Staniszewski, A. A. Stark, K. Vanderlinde, J. D. Vieira, R. Williamson, and O. Zahn, *Astrophys. J.* **716**, 1118 (2010).
- [47] K. Basu, Y.-Y. Zhang, M. W. Sommer, A. N. Bender, F. Bertoldi, M. Dobbs, H. Eckmiller, N. W. Halverson, W. L. Holzapfel, C. Horellou, V. Jaritz, D. Johansson, B. Johnson, J. Kennedy, R. Kneissl, T. Lanting, A. T. Lee, J. Mehl, K. M. Menten, F. P. Navarrete, F. Pacaud, C. L. Reichardt, T. H. Reiprich, P. L. Richards, D. Schwan, and B. Westbrook, *Astron. Astrophys.* **519**, A29 (2010).
- [48] C. L. Reichardt, O. Zahn, P. A. R. Ade, K. Basu, A. N. Bender, F. Bertoldi, H.-M. Cho, G. Chon, M. Dobbs, D. Ferrusca, N. W. Halverson, W. L. Holzapfel, C. Horellou, D. Johansson, B. R. Johnson, J. Kennedy, R. Kneissl, T. Lanting, A. T. Lee, M. Lueker, J. Mehl, K. M. Menten, M. Nord, F. Pacaud, P. L. Richards, R. Schaaf, D. Schwan, H. Spieler, A. Weiss, and B. Westbrook, *Astrophys. J.* **701**, 1958 (2009).
- [49] M. Nord, K. Basu, F. Pacaud, P. A. R. Ade, A. N. Bender, B. A. Benson, F. Bertoldi, H.-M. Cho, G. Chon, J. Clarke, M. Dobbs, D. Ferrusca, N. W. Halverson, W. L. Holzapfel, C. Horellou, D. Johansson, J. Kennedy, Z. Kermish, R. Kneissl, T. Lanting, A. T. Lee, M. Lueker, J. Mehl, K. M. Menten, T. Plagge, C. L. Reichardt, P. L. Richards, R. Schaaf, D. Schwan, H. Spieler, C. Tucker, A. Weiss, and O. Zahn, *Astron. Astrophys.* **506**, 623 (2009).
- [50] J. van der Kuur, J. Beyer, D. Boersma, M. Bruin, L. Gottardi, R. den Hartog, H. Hoevers, R. Hou, M. Kiviranta, P. J. de Korte, and B.-J. van Leeuwen, *Progress on Frequency-Domain Multiplexing Development for High Count rate X-ray Microcalorimeters*, in *AIP Conf. Proc.*, volume 1185, pages 245–248, 2009.
- [51] M. Dobbs, E. Bissonnette, and H. Spieler, *IEEE Trans. Nucl. Sci.* **55**, 21 (2008).
- [52] B. Benson *et al.* (The SPT Collaboration), *The South Pole Telescope Sunyaev Zel'dovich Receiver*, in preparation.
- [53] M. Lueker, B. A. Benson, C. L. Chang, H.-M. Cho, M. Dobbs, W. L. Holzapfel, T. Lanting, A. T. Lee, J. Mehl, T. Plagge, E. Shirokoff, H. G. Spieler, and J. D. Vieira, *IEEE Trans. Appl. Supercond.* **19**, 496 (2009).
- [54] J. Mehl, P. A. R. Ade, K. Basu, D. Becker, A. Bender, F. Bertoldi, H. M. Cho, M. Dobbs, N. W. Halverson, W. L. Holzapfel, R. Gusten, J. Kennedy, R. Kneissl, E. Kreysa, T. M. Lanting, A. T. Lee, M. Lueker, K. M. Menten, D. Muders, M. Nord, F. Pacaud, T. Plagge, P. L. Richards, P. Schilke, D. Schwan, H. Spieler, A. Weiss, and M. White, *J. Low Temp. Phys.* **151**, 697 (2008).
- [55] E. Shirokoff *et al.*, *IEEE Trans. Appl. Supercond.* **19**, 517 (2009).
- [56] E. Shirokoff, *The South Pole Telescope bolometer array and the measurement of secondary Cosmic Microwave Background anisotropy at small angular scales*, PhD the-

- sis, University of California, Berkeley, 2011.
- [57] C. E. Tucker and P. A. R. Ade, Thermal filtering for large aperture cryogenic detector arrays, in *Proc. SPIE Int. Soc. Opt. Eng.*, volume 6275, page 62750T, 2006.
- [58] P. A. R. Ade, G. Pisano, C. Tucker, and S. Weaver, A review of metal mesh filters, in *Proc. SPIE Int. Soc. Opt. Eng.*, volume 6275, page 62750U, 2006.
- [59] K. D. Irwin, *Appl. Phys. Lett.* **66**, 1998 (1995).
- [60] K. D. Irwin, G. C. Hilton, D. A. Wollman, and J. M. Martinis, *J. Appl. Phys.* **83**, 3978 (1998).
- [61] K. D. Irwin and G. C. Hilton, Transition-edge sensors, in *Cryogenic Particle Detection*, edited by C. Enss, volume 99, pages 63–149, Springer-Verlag, 2005.
- [62] T. Lanting, M. Dobbs, H. Spieler, A. T. Lee, and Y. Yamamoto, *Rev. Sci. Instrum.* **80**, 094501 (2009).
- [63] M. E. Huber, P. A. Neil, R. G. Benson, D. A. Burns, A. F. Corey, C. S. Flynn, Y. Kitaygorodskaya, O. Massihzadeh, J. M. Martinis, and G. C. Hilton, *IEEE Trans. Appl. Supercon.* **11(2)**, 4048 (2001).
- [64] J. C. Mather, *Appl. Opt.* **21**, 1125 (1982).
- [65] M. Lueker, *Measurements of Secondary Cosmic Microwave Background Anisotropies with the South Pole Telescope*, PhD thesis, University of California, Berkeley, 2010.
- [66] J. M. Lamarre, *Appl. Opt.* **25**, 870 (1986).
- [67] J. Zmuidzinas, *Appl. Opt.* **42**, 4989 (2003).
- [68] M. C. Runyan, *A search for galaxy clusters using the Sunyaev-Zel'dovich effect*, PhD thesis, California Institute of Technology, 2003.
- [69] F. Aubin, A. M. Aboobaker, P. Ade, C. Baccigalupi, C. Bao, J. Borrill, C. Cantalupo, D. Chapman, J. Didier, M. Dobbs, W. Grainger, S. Hanany, J. Hubmayr, P. Hyland, S. Hillbrand, A. Jaffe, B. Johnson, T. Jones, T. Kisner, J. Klein, A. Korotkov, S. Leach, A. Lee, M. Limon, K. MacDermid, T. Matsumura, X. Meng, A. Miller, M. Milligan, D. Polsgrove, N. Ponthieu, K. Raach, B. Reichborn-Kjennerud, I. Sagiv, G. Smecher, H. Tran, G. S. Tucker, Y. Vinokurov, A. Yadav, M. Zaldarriaga, and K. Zilic, First implementation of TES bolometer arrays with SQUID-based multiplexed read-out on a balloon-borne platform, in *Proc. SPIE Int. Soc. Opt. Eng.*, volume 7741, page 77411T, 2010.
- [70] K. Arnold, P. A. R. Ade, A. E. Anthony, F. Aubin, D. Boettger, J. Borrill, C. Cantalupo, M. A. Dobbs, J. Errard, D. Flanigan, A. Ghribi, N. Halverson, M. Hazumi, W. L. Holzapfel, J. Howard, P. Hyland, A. Jaffe, B. Keating, T. Kisner, Z. Kermish, A. T. Lee, E. Linder, M. Lungu, T. Matsumura, N. Miller, X. Meng, M. Myers, H. Nishino, R. O'Brient, D. O'Dea, C. Reichardt, I. Schanning, A. Shimizu, C. Shimmmin, M. Shimon, H. Spieler, B. Steinbach, R. Stompor, A. Suzuki, T. Tomaru, H. T. Tran, C. Tucker, E. Quealy, P. L. Richards, and O. Zahn, The POLARBEAR CMB polarization experiment, in *Proc. SPIE Int. Soc. Opt. Eng.*, volume 7741, page 77411E, 2010.
- [71] J. J. McMahon, K. A. Aird, B. A. Benson, L. E. Bleem, J. Britton, J. E. Carlstrom, C. L. Chang, H. S. Cho, T. de Haan, T. M. Crawford, A. T. Crites, A. Datesman, M. A. Dobbs, W. Everett, N. W. Halverson, G. P. Holder, W. L. Holzapfel, D. Hrubes, K. D. Irwin, M. Joy, R. Keisler, T. M. Lanting, A. T. Lee, E. M. Leitch, A. Loehr, M. Lueker, J. Mehl, S. S. Meyer, J. J. Mohr, T. E. Montroy, M. D. Niemack, C. C. Ngeow, V. Novosad, S. Padin, T. Plagge, C. Pryke, C. Reichardt, J. E. Ruhl, K. K. Schaffer, L. Shaw, E. Shirokoff, H. G. Spieler, B. Stadler, A. A. Stark, Z. Staniszewski, K. Vanderlinde, J. D. Vieira, G. Wang, R. Williamson, V. Yefremenko, K. W. Yoon, O. Zhan, and A. Zenteno, SPTpol: an instrument for CMB polarization, in *AIP Conf. Proc.*, edited by B. Young, B. Cabrera, & A. Miller, volume 1185, pages 511–514, 2009.
- [72] M. Dobbs, F. Aubin, T. de Haan, S. Hanany, N. Harrington, W. Holzapfel, K. Hubmayr, A. Lee, M. Lueker, K. MacDermid, and S. Smecher, *J. Low Temp. Phys.* **167** 568-574 (2012) .
- [73] T. de Haan, G. Smecher, and M.A. Dobbs, Improved Performance of TES Bolometers using Digital Feedback, to appear in in *Proc. SPIE Int. Soc. Opt. Eng.* (2012).
- [74] S.-F. Lee, J. M. Gildemeister, W. Holmes, A. T. Lee, and P. L. Richards, *Appl. Opt.* **37**, 3391 (1998).